Fall 2012

Mantle flow and lithosphere-asthenosphere coupling beneath the southwestern edge of the North American craton: constraints from shear-wave splitting measurements

Hesham A. Refayee

Department: Geosciences and Geological and Petroleum Engineering

MANTLE FLOW AND LITHOSPHERE-ASTHENOSPHERE COUPLING BENEATH THE SOUTHWESTERN EDGE OF THE NORTH AMERICAN CRATON: CONSTRAINTS FROM SHEAR-WAVE SPLITTING MEASUREMENTS

by

HESHAM AHMAD REFAYEE

A DISSERTATION

Presented to the Faculty of the Graduate School of the

MISSOURI UNIVERSITY OF SCIENCE AND TECHNOLOGY

In Partial Fulfillment of the Requirements for the Degree

DOCTOR OF PHILOSOPHY

in

GEOLOGY AND GEOPHYSICS

2012

Approved by:

Kelly Liu, Co-Advisor
Stephen Gao, Co-Advisor
John Hogan
Mohamed Abdelsalam
Kevin Mickus
Andreas Eckert

PUBLICATION DISSERTATION OPTION

Pages 1, 3-11, 14, 15, 28-52, and 77-82 have been submitted to the Earth and Planetary Science Letters journal.

ABSTRACT

High-quality broadband seismic data recorded by the USArray and other stations in the southwestern United States provide a unique opportunity to test different models of anisotropy-forming mechanisms in the vicinity of a cratonic edge. Systematic spatial variations of anisotropic characteristics are revealed by 3027 pairs of splitting parameters measured at 547 broadband seismic stations. The western and southern edges of the North American craton show edge-parallel fast directions with larger-than-normal splitting times, and the continental interior is characterized by smaller splitting times spatially consistent fast directions that are mostly parallel to the absolute plate motion direction of North America. Except for a small area in the vicinity of the Llano Uplift in central Texas, no systematic azimuthal variations of the splitting parameters are observed, suggesting that a single layer of anisotropy with horizontal axis of symmetry can adequately explain the observations. Estimation of the depth of the source of the observed anisotropy using spatial coherency of the splitting parameters indicates that the observed anisotropy mostly originate from the upper asthenosphere, through simple shear between the partially coupled lithosphere and asthenosphere.

ACKNOWLEDGMENTS

I would like to express the deepest appreciations to my committee chairs, Dr. Kelly Liu and Dr. Stephen Gao, who have the attitude and the substance of genius. They continually and convincingly conveyed a spirit of adventure in regard to research, and an excitement in regard to teaching. Without their guidance and persistent assistance this dissertation would not have been possible.

I would like to thank my committee members, Dr. John Hogan and Dr. Mohamed Abdelsalam for their constant inspiration, encouragement, and advice. They have taught me everything I need to know about field geology techniques. My sincere appreciation also goes to Dr. Kevin Mickus for accepting to be a member in my committee.

I would like to extend my thankfulness to my family for their support and prayers throughout my study. My sincere gratitude goes to my father, my mother, brothers, and sisters.

My ultimate and most heartfelt go to my wife, Khadija, and my little son Ahmad for their support, sacrifice, and patience. They made life so easy for me.

TABLE OF CONTENTS

LIST OF ILLUSTRATIONS

NOMENCLATURE

Symbol	Description
ϕ	Fast polarization direction
δt	Splitting time delay
Fv	Spatial variation factor

1. INTRODUCTION

Shear-wave splitting (SWS) analysis is one of the most commonly used techniques in structural seismology. The two resulting splitting parameters, the polarization direction of the fast wave (Φ or fast direction) and the arrival time difference between the fast and slow waves (δt or splitting time), are respectively indicators of the orientation and strength of seismic anisotropy accumulated along the ray path. The P-to-S converted waves at the core mantle boundary (XKS, which includes SKS, SKKS, and PKS) are ideal for SWS analysis, due to the fact that the initial polarization direction is along the radial direction and thus any energy in the XKS window on the transverse component is an indicator of azimuthal anisotropy (Silver and Chan, 1991) (Figure 1.1).

While the splitting parameters can usually be reliably determined, at the present time, the interpretation of the resulting splitting parameters is still an unsettled and debated issue. Numerous laboratory and modeling studies confirmed that lattice preferred orientation (LPO) of the crystallographic axes of olivine is the main cause of mantle anisotropy. Except for areas with extreme anomalies in temperature, pressure, and 48 water contents, these studies suggested that the fast direction is subparallel to the LPO of the a-axis of olivine (Zhang and Karato, 1995; Karato et al., 2008).

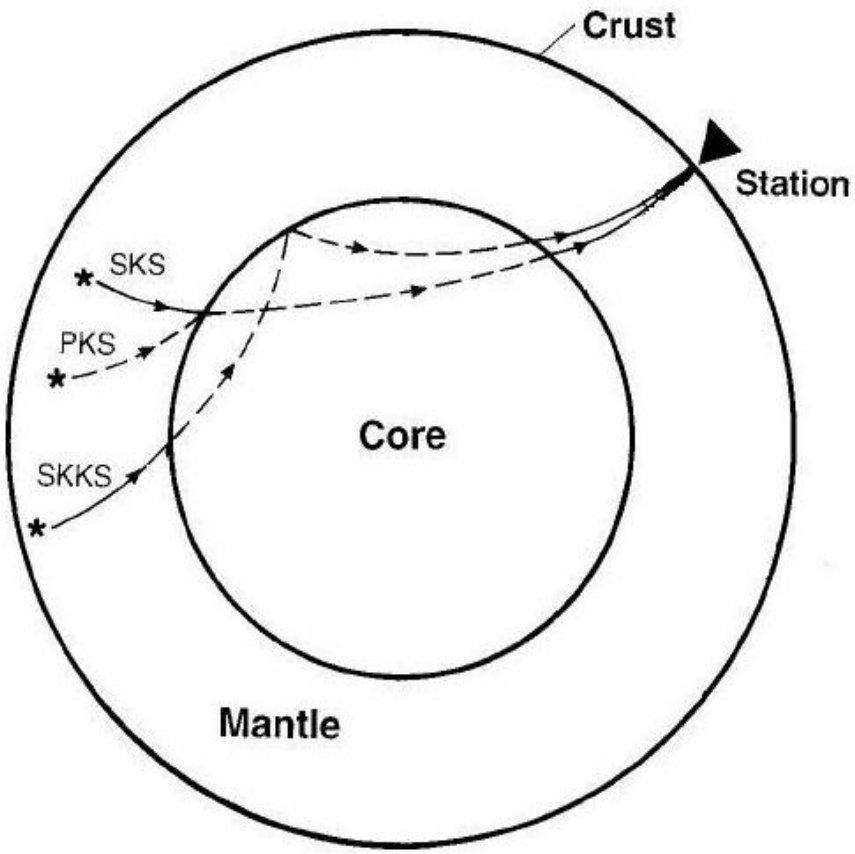

Figure 1.1. Propogation wave path of the seismic phases used to characterize the mantle anisotropy. XKS phases convert at the Core-Mantle Boundary (CMB). P-to-S converted waves at CMB including SKS, SKKS, and PKS are commonly used to qualify seismic anisotropy (Savage, 1996).

Unfortunately, there are more than one mantle processes that can lead to the LPO, among which the most important ones are simple shear originated from the gradient of flow in the asthenosphere which lead to a fast direction that is parallel to the flow direction, and lithospheric compression which results in anisotropy with a fast direction parallel to the strike of the mountain belts (Silver, 1996; Savage, 1999; Fouch and Rondenay, 2006; Long and Silver, 2009). Adding to this ambiguity in the interpretation of SWS measurements is the hypothesis that magmatic dikes in the lithosphere, when aligned preferably along a certain direction, can also lead to observable seismic anisotropy with a dike-parallel fast direction (Gao et al., 1997; Kendall et al., 2005) (Figure 1.2).

Therefore, whether seismic anisotropy observed in a given area is lithospheric or asthenospheric origin (and whether it is compression origin or dike origin if it is in the lithosphere) is the key information needed for useful interpretation of the SWS measurements. Unfortunately, due to the steep angle of incidence of the XKS waves, the vertical resolution of the SWS technique is low.

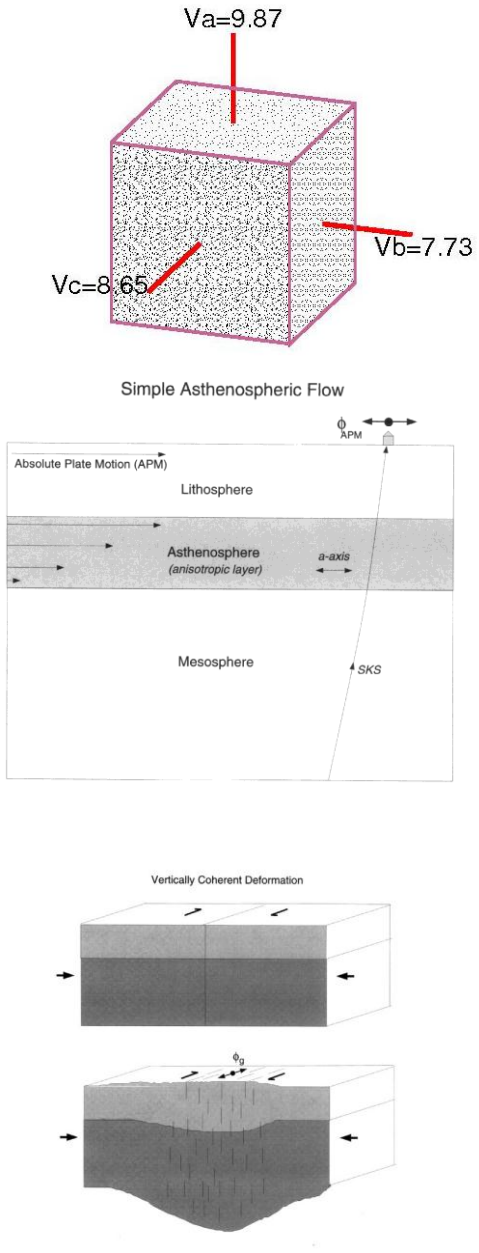

Figure 1.2. Possible causes of mantle anisotropy. Top panel), Shear wave velocities in monocrystal of olivine. Middle panel), Cross-section of simple Asthenospheric flow; the fast direction is parallel to the flow direction. Lower panel), Schematic of vertical coherent deformation where fast directions are parallel to mountain belts (Silver, 1996).

To some extent, surface wave dispersion studies can resolve the depth distribution of seismic anisotropy (Montagner, 1998; Yuan and Romanowicz, 2010), but the resolution in both vertical and horizontal directions is intrinsically low. Recently, Liu and Gao (2011) proposed a procedure to estimate the depth of the source of anisotropy using spatial variation of splitting parameters. This technique requires the availability of high-quality SWS measurements obtained at densely spaced seismic stations.

As discussed below, the study area (Figure 1.3) is well sampled by stations in the ongoing USArray project, which has a nominal station spacing of 70 km and has recorded an outstanding data set for characterizing 3-D distribution of seismic anisotropy in the mantle beneath the study area. Another issue that can be constrained using SWS analysis is the degree of coupling between the lithosphere and the underlying asthenosphere.

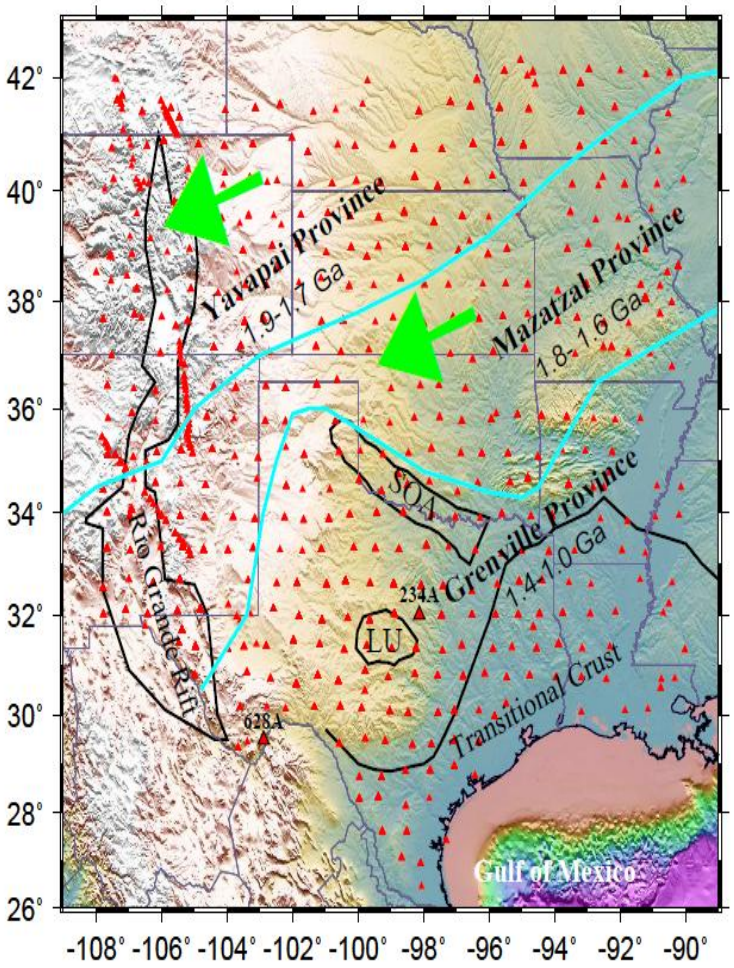

Figure 1.3. Topographic relief map of the study area showing seismic stations used in the study (triangles) and major tectonic provinces. The solid blue lines separate Precambrian basement terranes (Thomas, 2006), and the green arrows indicate the direction of the absolute plate motion (APM) of the North American Plate (Gripp and Gordon, 2002). Example data from the two named stations (234A and 628A) are shown in Figure 3. SOA: Southern Oklahoma Aulacogen; LU: Llano Uplift.

Global scale anisotropy studies using surface waves suggested that the asthenosphere beneath most slow-moving continents is nearly isotropic, implying decoupling between the lithosphere and asthenosphere except for Australia which is the fastest moving continent (Debayle et al., 2005). Decoupling is also advocated by others to explain westward net drift of the lithosphere relative to the asthenosphere (Doglioni et al., 2011), and to explain geoid anomalies across transform faults that separate ocean floors of different age (Craig and McKenzie, 1986). Most of these studies proposed the existence of an ultra-thin, low viscosity layer immediately beneath the lithosphere. This layer prevents transfer of shear stress between the lithosphere and the asthenosphere, leading to decoupling of the two. However, some geodynamic modeling and seismic anisotropy studies suggested a high-degree coupling between the two layers (Becker and O'Connell, 2001; Marone and Romanowicz, 2007; Bird et al., 2008).

A combination of the broadband seismic data set and the tectonic setting of the study area provide an excellent opportunity to address this problem. The bulk of the study area consists of the southeastern part of the western US orogenic zone, the southern Great Plains, and the transition zone between the two (Figure 1.3). Two suture zones divide the Proterozoic basement into three provinces, which become progressively younger 98 toward the southeast (Thomas, 2006; Whitmeyer and Karlstrom, 2007). Major tectonic features include the Rio Grande Rift, the Southern Oklahoma Aulacogen, and the continental-oceanic transitional crust formed as a result of extension during the formation of the Gulf of Mexico (Mickus et al., 2009). Seismic body wave and surface wave tomography (van der Lee and Nolet, 1997; Yuan and Romanowicz, 2010; Burdick et al.,

2012) suggest that the lithosphere beneath the Great Plains has a thickness of about 200-250 km, and thins to about 125 km beneath the western US orogenic zone and beneath the area with transitional crust (Wilson et al., 2005; van der Lee and Frederiksen, 2005; Yuan and Romanowicz, 2010).

1.1. Tectonic setting and previous seismic anisotropy studies

The southwest part of the contiguous United States has experienced significant amount of deformation, magmatism, and extension from the Precambrian to the Cenozoic Era (Whitmeyer and Karlstrom, 2007; Karlstrom and Bowring, 1988). These orogenic events include the late 122 Proterozoic Yavapai orogeny (1.71-1.68 Ga), the Mazatzal orogeny (1.7-1.65 Ga), and Grenville orogeny (1.3-0.9 Ga) (Whitmeyer and Karlstrom, 2007). During the Proterozoic, the basement of the continental crust was rapidly generated by the accretion of several major volcanic arcs (Hoffman, 1988; 1989; Condie, 1982; Karlstrom and Bowing, 1988).

The widespread extension which took place during the Cenozoic time (Coward et al., 1987) created magmatic episodes in the Tertiary Period (Baldridge at al., 1991; Balch et al., 1997; McMillan et al., 2000), uplifted the Colorado Plateau (Liu and Gurnis, 2010) and caused the rifting of the Rio Grande Rift during the Grenville orogeny (Morgan et al., 1986; Mosher, 1998; Lawton and McMillan, 1999). In the study area, several SWS and other seismic anisotropy studies were conducted during the pre-USArray era. Consequently the spatial coverage was limited related to that presented here. A study conducted by Savage and Sheehan (2000) measured SKS splitting using data from the Colorado Plateau-Great Basin portable Array stations.

They observed NE-SW fast direction beneath both the Rio Grande Rift and the Rocky Mountains with a splitting time of 1.0 s. A mantle flow around the keel was proposed by Fouch et al. (2000) based on shear wave splitting observation from eastern US obtained from two arrays (MOMA, and NOMAD) of 22 broadband stations.

Barruol et al. (1997) explained the large scale of anisotropy pattern around the southern margin of stable North America by asthenospheric flow that is deflected around the thick North American craton. Sandval et al. (1992) reported the N-S fast polarization direction beneath the Rio Grande Rift obtained from five temporary digital stations. Wang et al. (2008) have also indicated that the fast polarization directions have N to NE orientation within the south eastern rim of the rift. Splitting time of 1.4 s was found by Gok et al. (2003) in the same area with similar patterns of fast directions.

Gao et al. (2008) conducted shear wave splitting measurements at permanent broadband stations in the south-central United States. They attributed magmatic dikes in the lithosphere and/or asthenospheric flow for the observed anisotropy. In the study area, using joint inversion surface waveform and a limited number of SKS splitting measurements, Yuan and Romanowicz (2010) proposed two distinct layers. The upper layer, which resides in the lithosphere, has a N-S fast direction, and the lower layer,which is in the upper asthenosphere, is dominated by NE-SW fast directions.

2. Data and Methods

The study area ranges from 109◦W −90◦W and 26◦N−42◦ N. Broadband seismic data from all the USArray and permanent stations in the study area were requested from the IRIS (Incorporated Research Institutions for Seismology) DMC (Data Management Center). For stations on the western US orogenic zone (approximately west of 105◦ W) where rapid spatial variation of anisotropy is expected, we also requested data from portable seismic experiments. Data from most of the stations ended around early 2012. The cutoff magnitude for events with a focal depth _ 100 km is 5.6, and that for deeper event is 5.5 to take the advantage of the sharper waveforms normally associated with deep events. The epicentral distance range used is 120◦ -180◦ for PKS, and 84◦ - 180◦ for SKKS and SKS (Gao and Liu, 2009).

Following the procedure of Liu (2009) (Figure 1.4), which was based on the minimization of transverse energy approach of Silver and Chan (1991), we resampled the seismograms into a uniform sampling rate of 20 sps, and band-pass filtered them in the frequency band of 0.04-0.5 Hz which contains most of the XKS energy. All the measurements were visually inspected and if necessary, data processing parameters such as the beginning and ending time of the XKS window, band-pass filtering parameters, and automatically determined ranking (Liu et al., 2008) were adjusted manually (Figure 1.5). Figures 1.3 and 1.6 show the distribution of the stations and the events, respectively, and Figure 1.7- 1.19 shows examples of XKS phases and various figures associated with the data processing procedure.

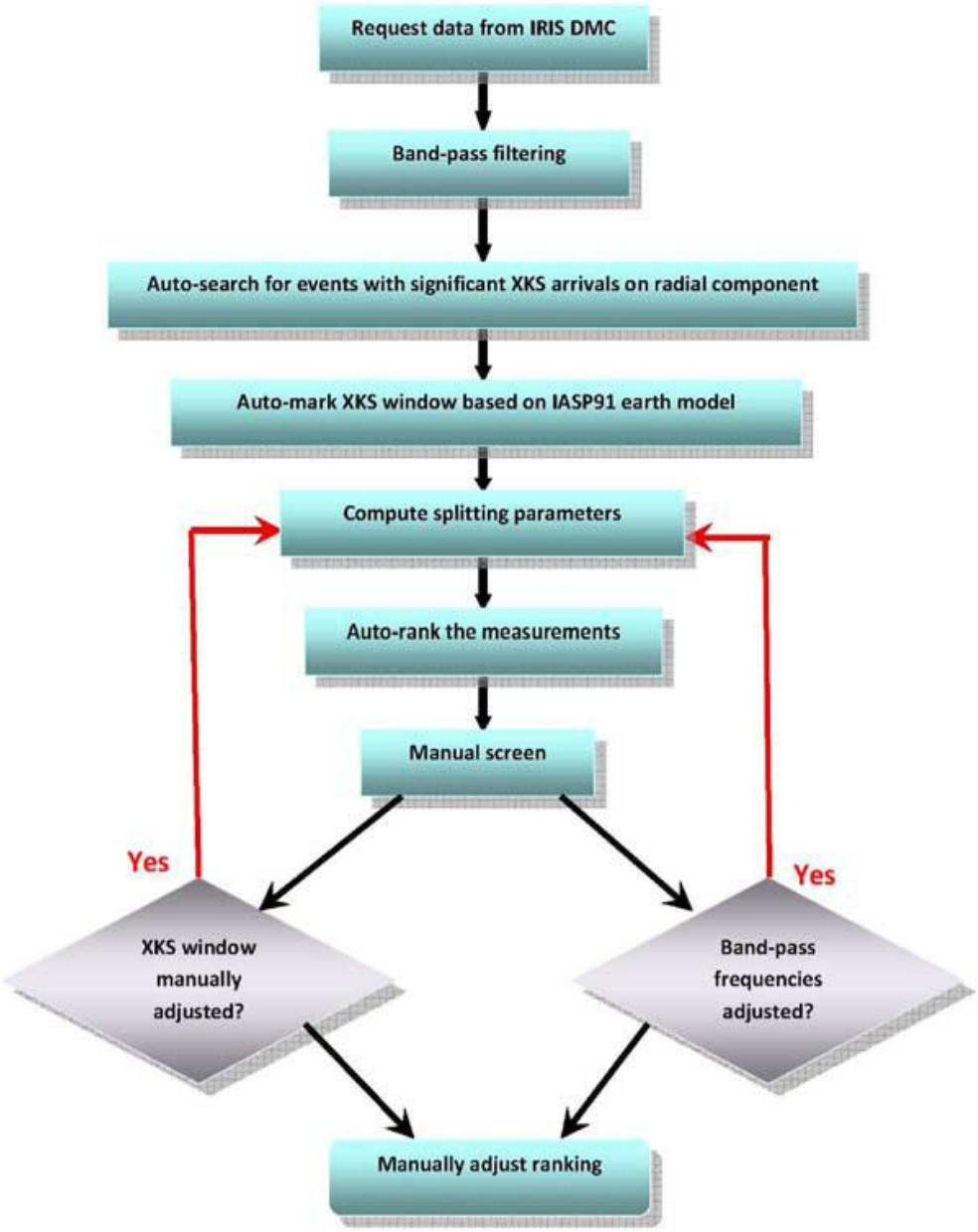

Figure 1.4. A flowchart showing the procedure for measuring, verifying, and ranking shear wave splitting parameters used in this study (Liu, 2009).

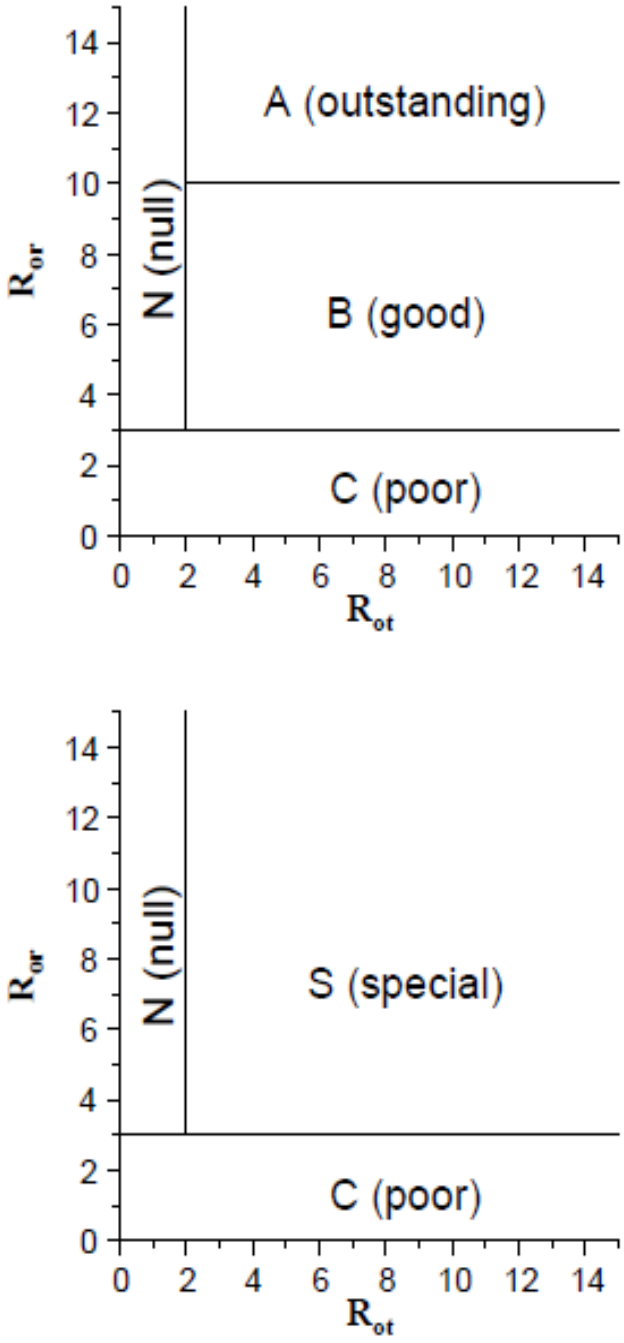

Figure 1.5. Ranking chart for the XKS splitting results. Ror is signal-to-noise ratio on the original radial component; Rot is signal-to-noise ratio on the original transverse component. (top) For Rct/Rot _ 0.7. (bottom) For Rct/Rot > 0.7, where Rct is the S/N on the corrected transverse component (Liu et al., 2008).

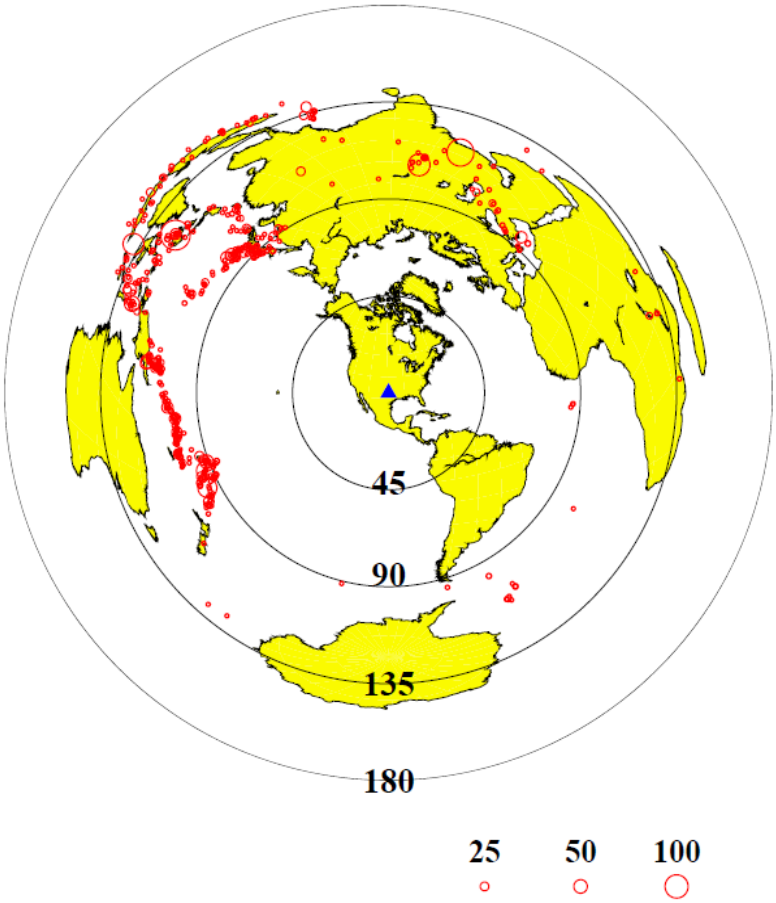

Figure 1.6. An azimuthal equidistant projection map showing the distribution of 475 earthquakes used in the study. Size of the red circles is proportional to the number of resulting well-defined splitting measurements. The black circles and corresponding labels show the distance in degree to the center of the study area.

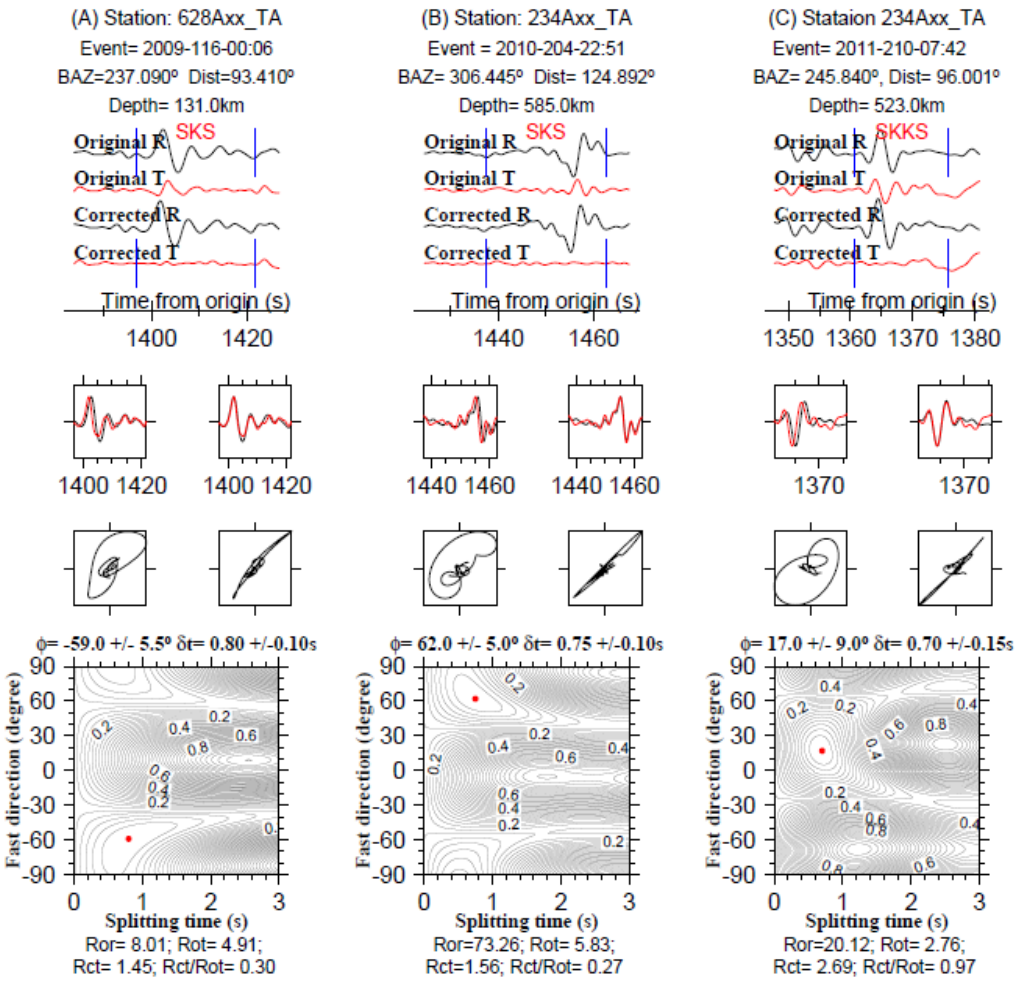

Figure 1.7. Original and corrected XKS seismograms (top panels), particle motion patterns (middle), and the contour maps of transverse component energy (bottom) from stations 628A TA (A) and 234A TA (B and C). The red dot on the contour map indicates the optimal splitting parameters.

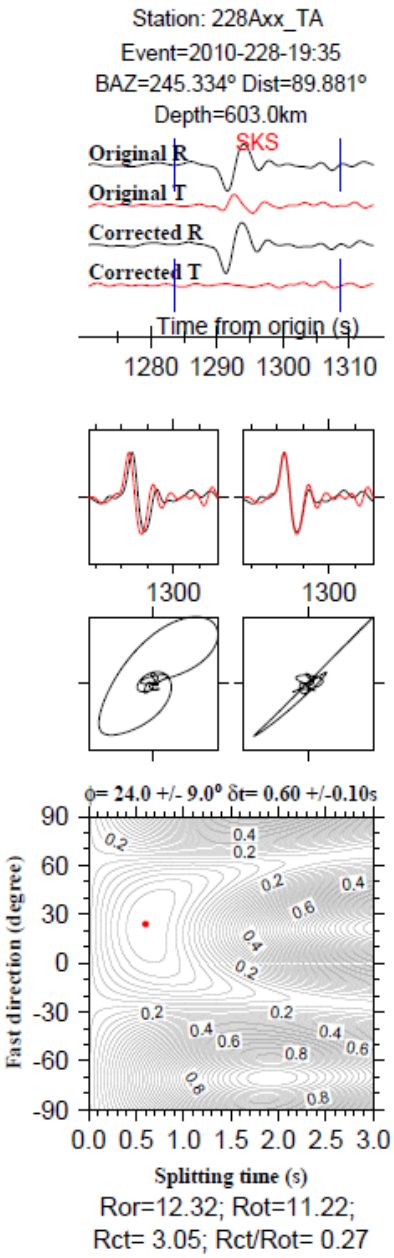

Figure 1.8. An example of SKS measurement from station 228A in area **A**. Original and corrected radial and transverse components (top panels), their particle motion (middle panel), and Contour map of normalized energy on the corrected transverse component (bottom panel). The vertical thick blue lines are "a" and "f" positions and represent the time window on which shear wave splitting parameters is made. The red dot in the map refers to the optimal shear wave splitting parameters.

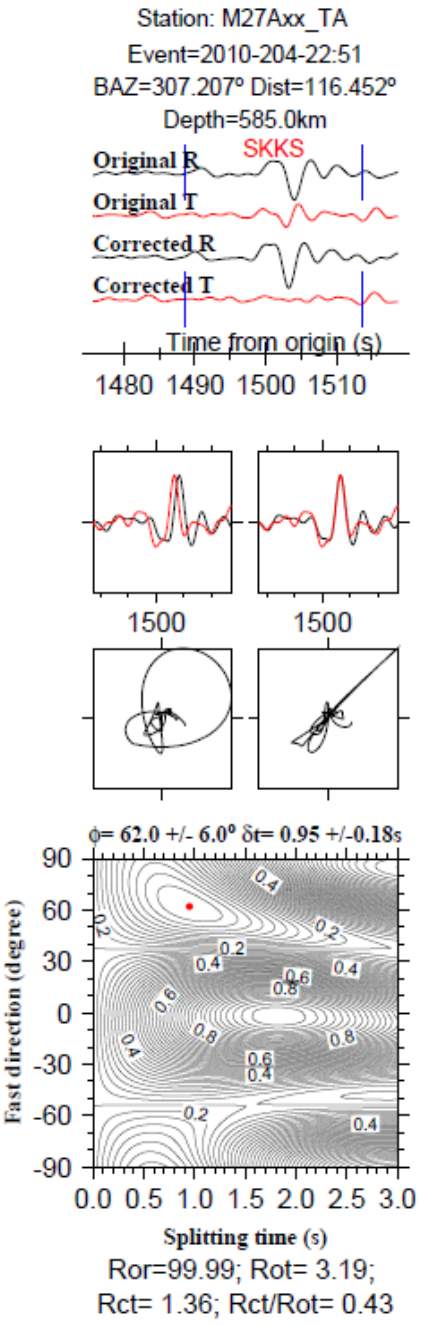

Figure 1.9. Same as Figure 1.8 but for a SKKS phase recorded by station M27A from area A

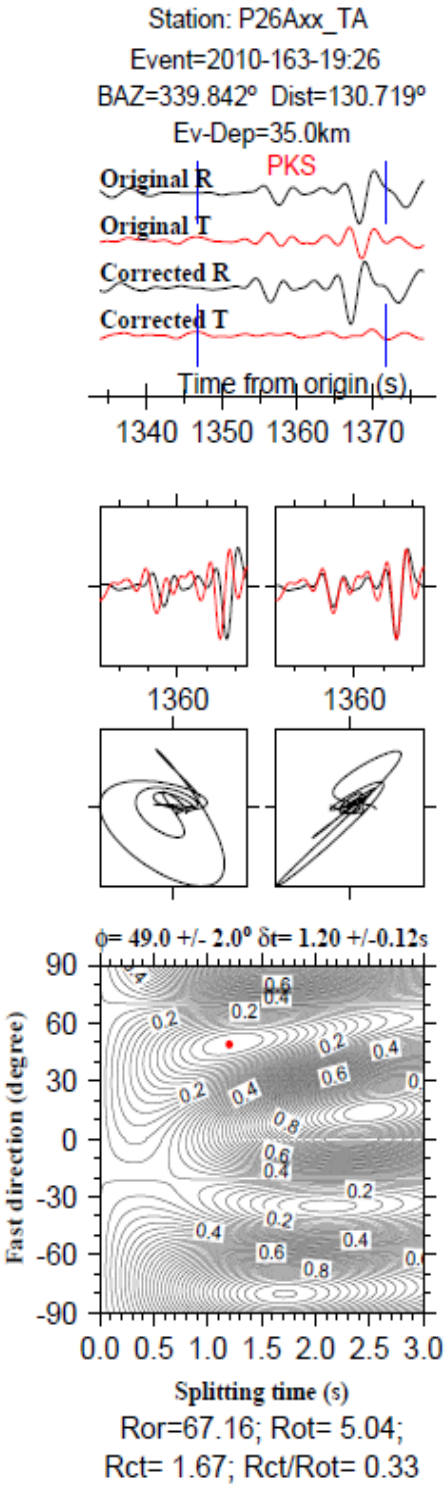

Figure 1.10. Same as Figure 1.8 but for a PKS phase recorded by station P26A from area A

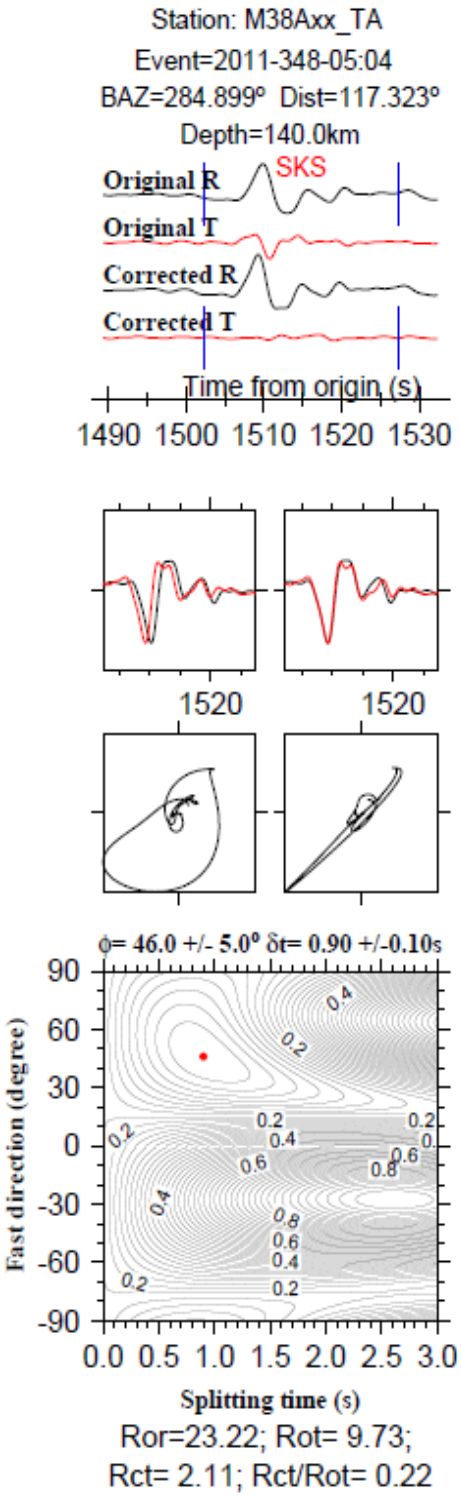

Figure 1.11. Original and corrected seismogram for SKS recorded by station M38A from area B

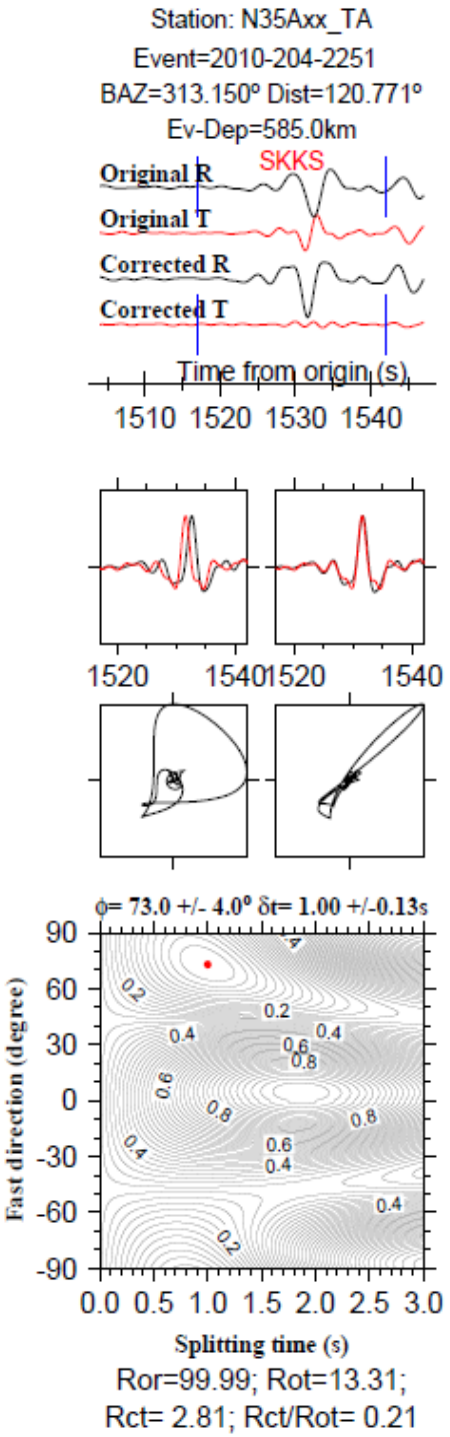

Figure 1.12. Same as Figure 1.11, but for SKKS recorded by station N35A from area B

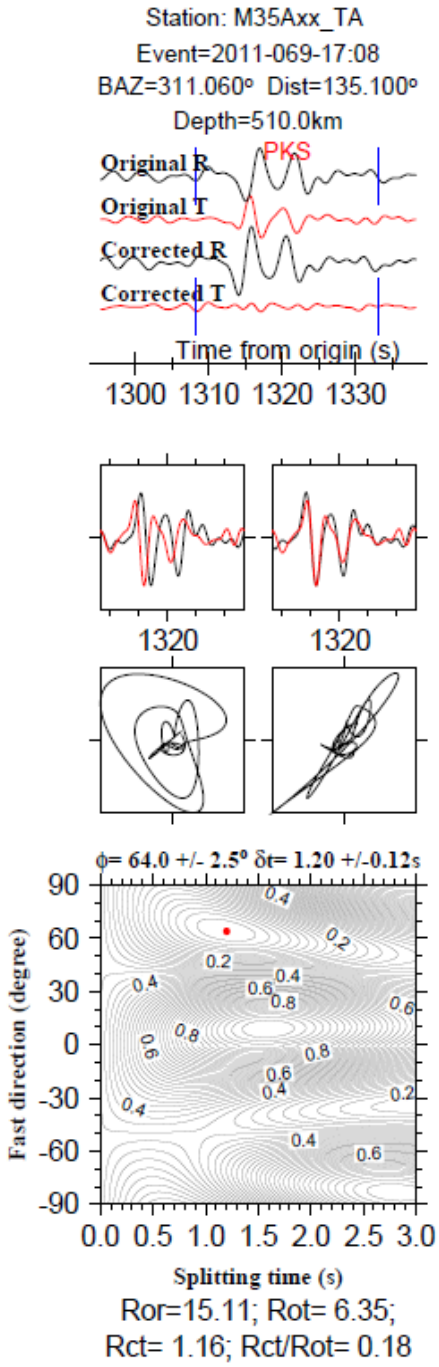

Figure 1.13. Same as Figure 1.11, but for PKS recorded by station M35A from area B

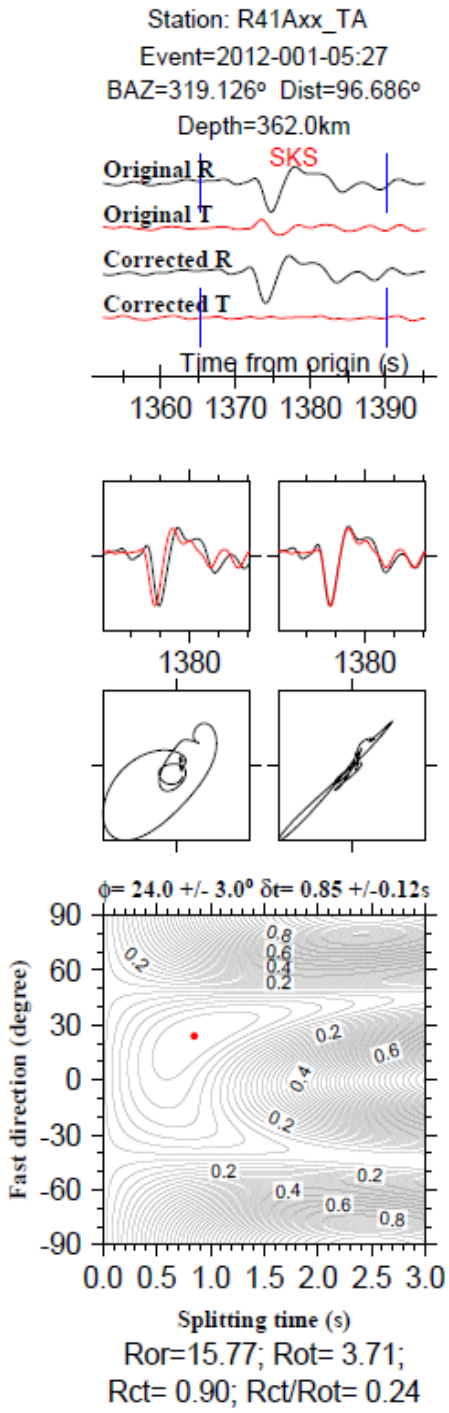

Figure 1.14. Original and corrected seismogram for SKS recorded by station R41A from area C

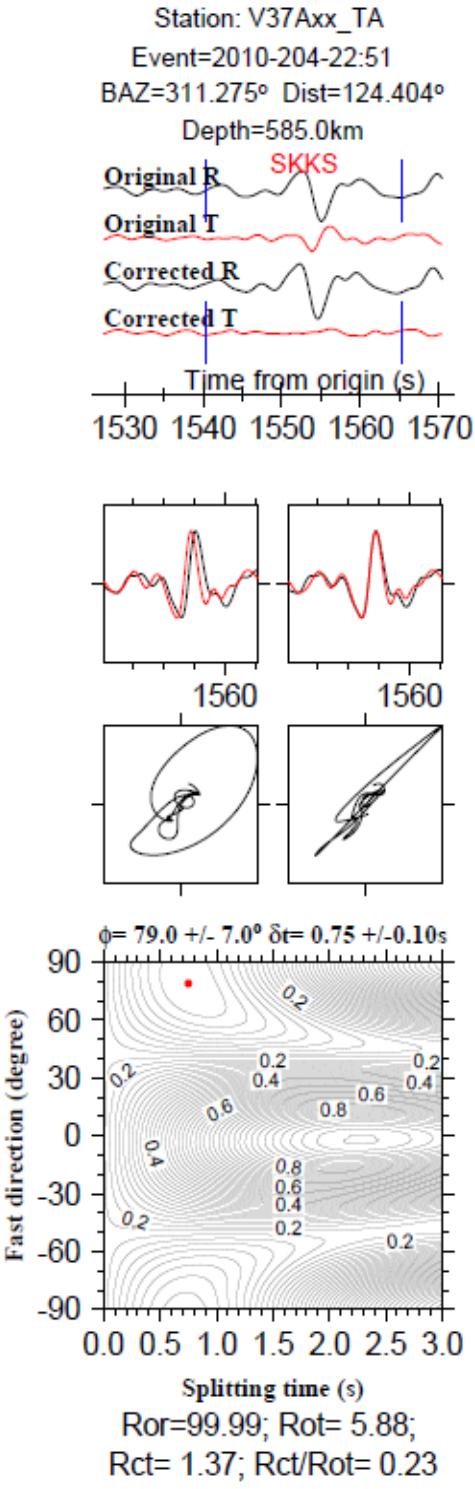

Figure 1.15. Same as Figure 1.14, but for SKKS recorded by station V37A from area C

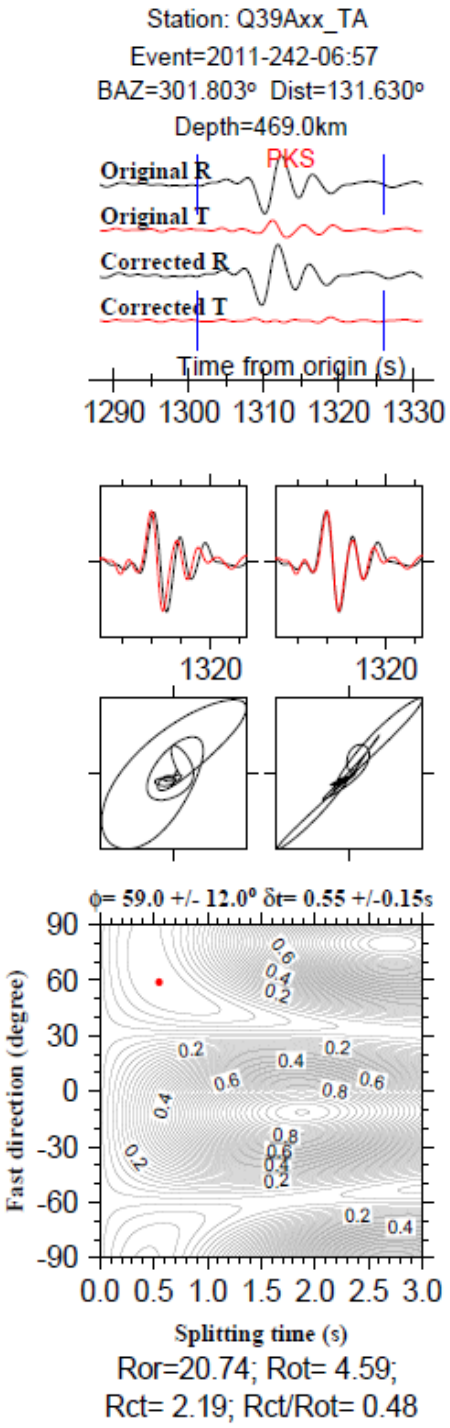

Figure 1.16. Same as Figure 1.14, but for PKS recorded by Q39A for area C

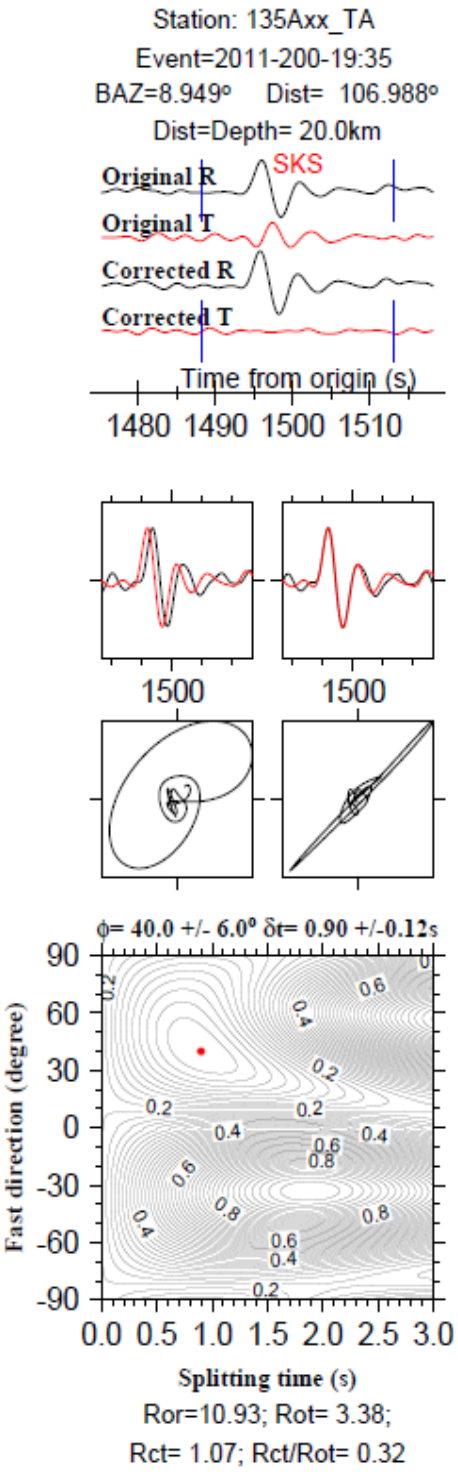

Figure 1.17. Original and corrected seismogram for SKS recorded by 135A from area D

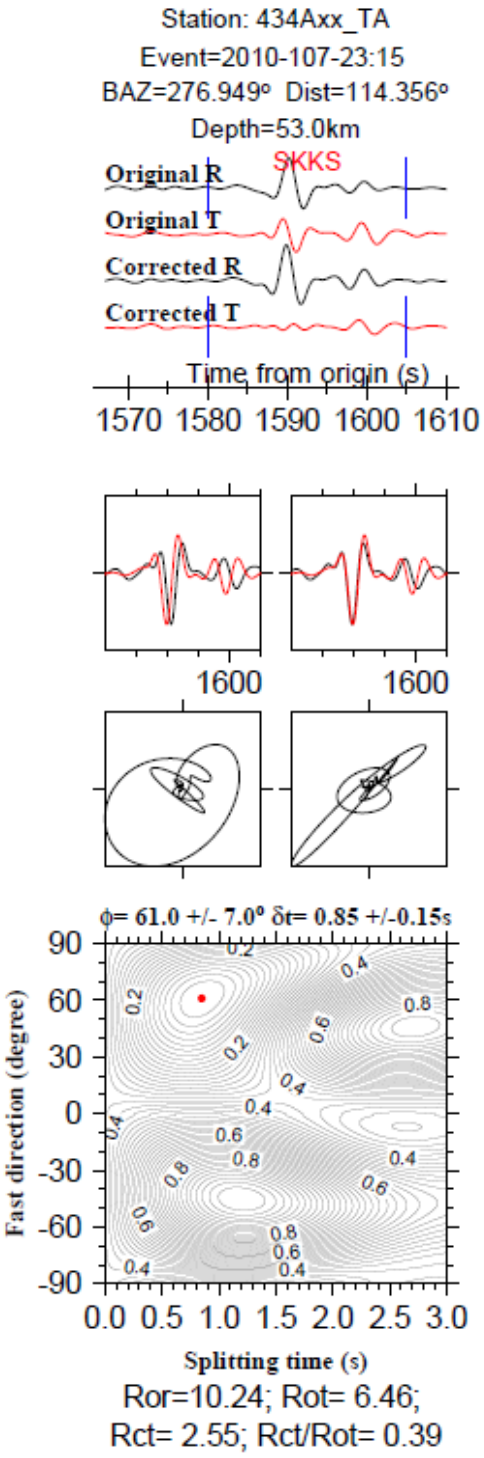

Figure 1.18. Same as Figure 1.17, but for SKKS recorded by station 434A from area D

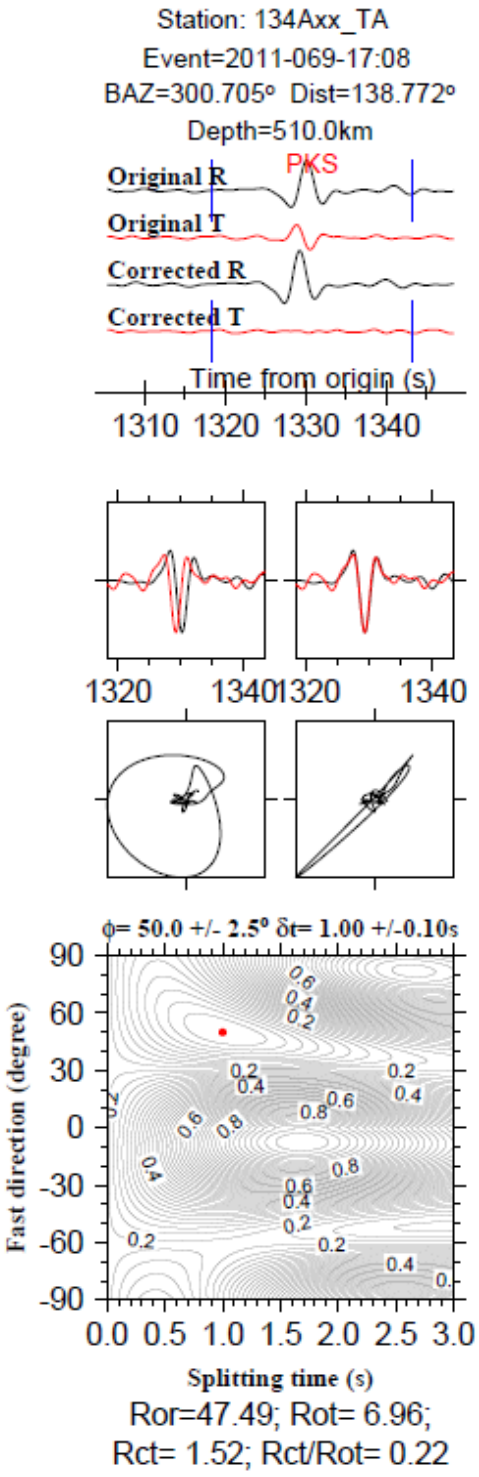

Figure 1.19. Same as Figure 1.17, but for PKS recorded by station 134A from area D

3. Results

3.1. Spatial variations of resulting splitting parameter

A total of 3027 pairs of well-defined (Quality A and B, see Liu et al., 2008 for details about ranking criteria) splitting parameters were obtained from 475 events at 547 stations. Among the measurements 2238 are SKS, 406 are SKKS, and 383 are PKS measurements. The mean splitting time over all the measurements is 1.01±0.34 s which is identical to the global average of 1.0 s (Silver, 1996). For a commonly-assumed degree of anisotropy of 4% (Mainprice et al., 2000), the thickness of the anisotropic layer is about 110±30 km. In the following we quantify the spatial and azimuthal variations of the splitting parameters.

The resulting SWS parameters (Figures 3 and 4) show systematic spatial variations and close correspondence with the absolute plate motion (APM) direction and geological provinces. Fast directions observed on the western US orogenic zone and its transition zone with the Great Plains are dominantly N-S, while the rest of the study area shows mostly NE-SW fast directions (Figure 3). We divide the study area into four areas based on the characteristics of the SWS measurements and also on Proterozoic basement provinces. Area A, which contains 1388 pairs of measurements from 253 stations, is the east-most portion of the western US orogenic 195 zone and its transition zone with the Great Plains. The shear wave The mean fast directions in this area is 28±23.4◦, and the mean splitting time is 1.05± 0.35 s.

Area B is the southern part of the Yavapai province and contains 421 pairs of SWS measurements from 62 stations. The mean fast direction is 64±22◦, and the mean splitting time is 0.89 ± 0.28 s. Area C is the Mazatzal province and contains 367 pairs of measurements from 87 stations, and the mean splitting parameters are 57±25◦ and 0.86±0.29 s. Area D is the Grenville province. The southern part of this area is covered by continental-oceanic transitional crust. This area has 851 pairs of measurement from 145 stations. The mean splitting time of 1.15±0.36 s is the largest among the four areas, and the mean fast direction is 63±21◦.

3.2. Fast directions

To illustrate the spatial variation of the fast directions and to explore their relationship with the APM direction, we calculate the APM direction for each of the 3027 ray-piercing points (at the depth of 200 km) based on the fixed hot-spot model of Gripp and Gordon (2002), and obtain the absolute difference between the two directions in the range of 0◦ to 90◦. The resulting differences are then spatially averaged in 1◦ by 1◦ blocks and resampled into a finer resolution of 0.1◦ using the grdsample function in Generic Mapping Tools (Wessel and Smith, 1991) for display (Figure 1.20).

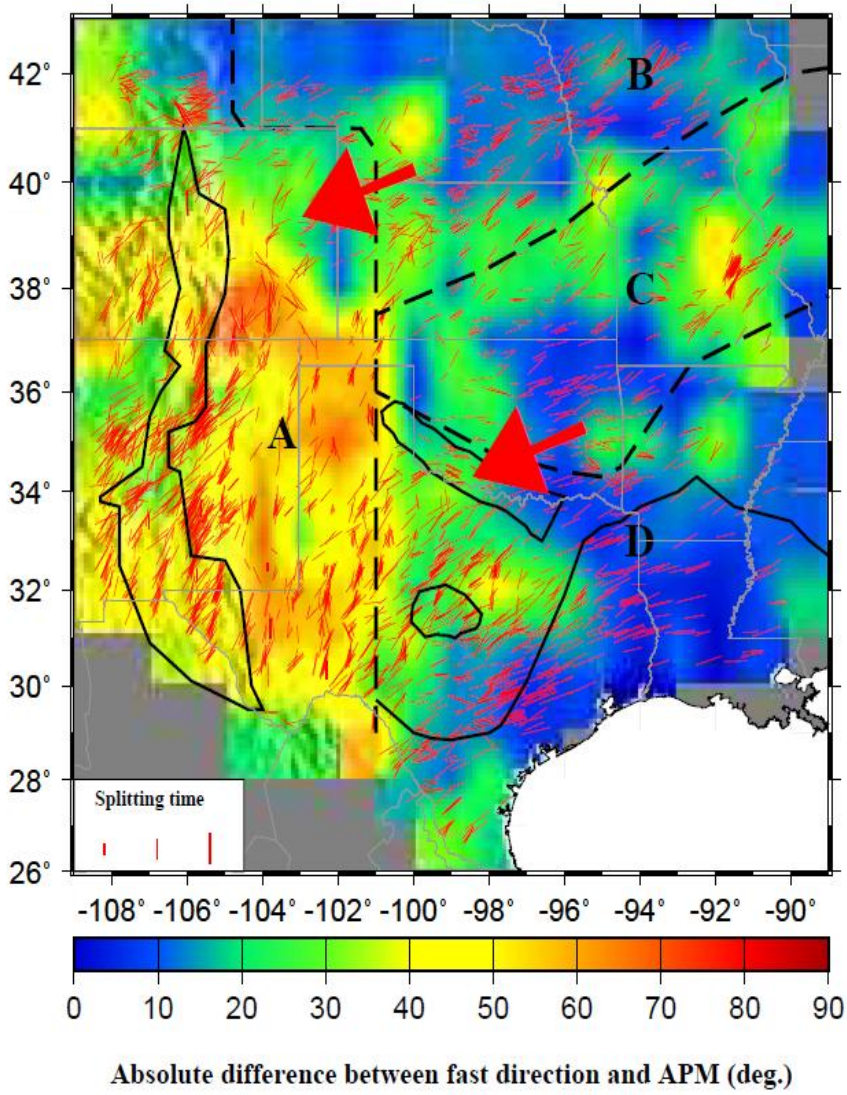

Figure 1.20. Well-defined shear-wave splitting measurements. The orientation of the red bars represents the fast polarization direction, and the length is roportional to the splitting time. The background image shows absolute difference between the observed fast directions and the APM (red arrows). The dashed lines separate areas with distinct basement ages and/or tectonic history.

The resulting image (Figure 1.20) indicates that beneath the western US Orogenic zone and its transition area with the Great Plains, the fast directions are almost orthogonal with the APM direction. On the contrary, the fast directions and the APM are largely consistent beneath the Great Plains and the transitional crust, with a few exceptions. The first is an area centered at (98◦W, 32◦ N) in central Texas, tectonically known as the Llano Uplift (Mosher, 1998). The fast directions in this area are more northerly and spatially vary. As discussed in the next section, this apparent deviation of the fast direction from the APM direction is caused by azimuthal variations of the splitting parameters as a result of double layer anisotropy. The second area with large deviations is a band along the boundary between the Yavapai and Mazatzal provinces (Figure 1.20). This band departs from the boundary at about 95◦ W and extends eastward.

The large deviations are caused by the fact that the fast directions are spatially less consistent relative to the other areas of the Great Plains. The third area, although not as profound as the two above, is located at the south-most tip of Texas. The measurements in this area are more northerly than the rest of the stations on the transitional crust. This observation, when combined with the relatively small splitting times in this area (Figure 1.21) and the shape of the edge of the North American continent, has important significance about the flow pattern around the cratonic keel, as detailed in the Discussion section below. Finally, the 6 measurements at the south-most tip of the Rio Grande Rift are mostly E-W oriented (Figure 1.20), suggesting a possible termination of the N-S domain to the north. Figure 1.7A shows an example of these measurements.

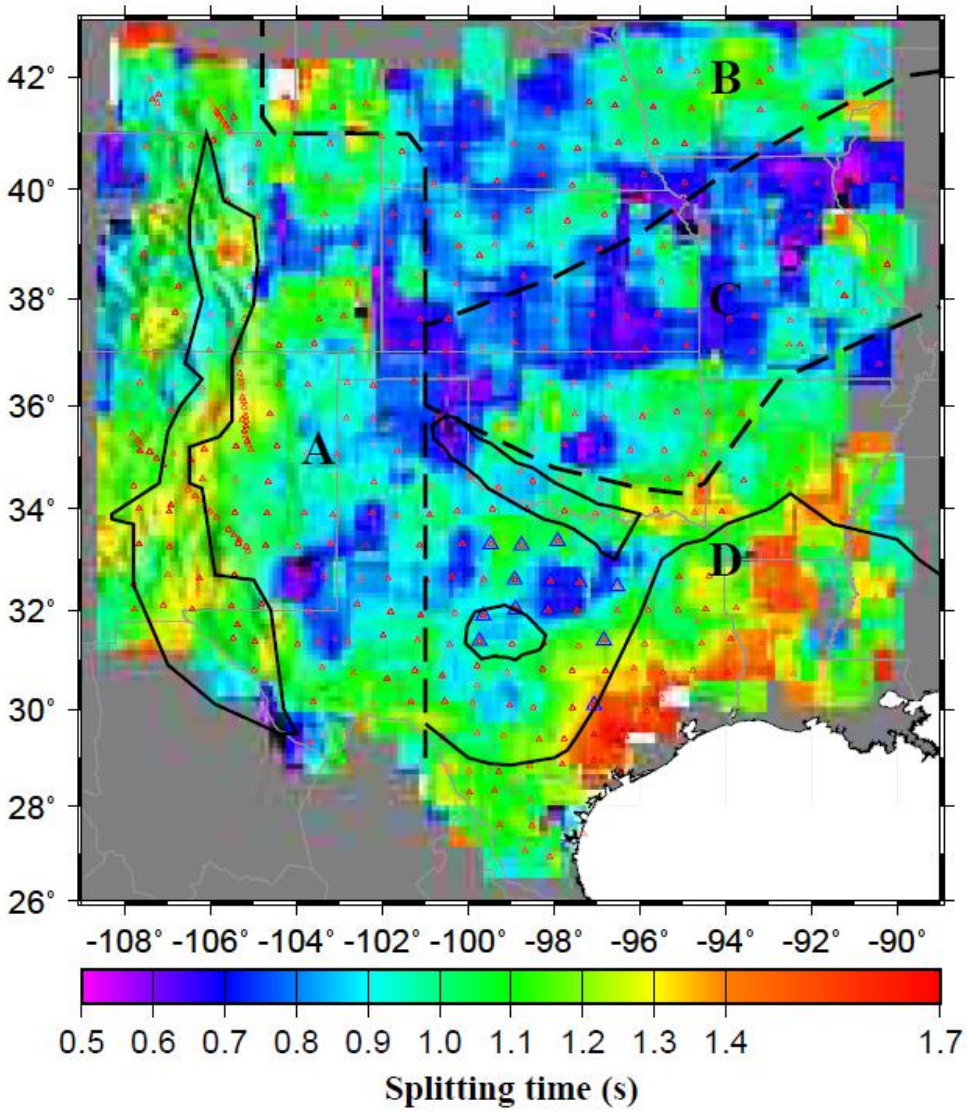

Figure 1.21. Spatial distribution of splitting times. Red triangles represent seismic stations used in the study. Dashed lines represent boundaries between the four areas. Stations represented by blue triangles show systematic azimuthal variation of splitting parameters shown in Figure 1.22.

3.3. Splitting times

The spatial distribution of splitting times shown in Figure 1.21 was produced by averaging the individual splitting times at the piercing points of 200 km deep in overlapping 1◦ by 1◦ blocks, and by resampling to a resolution of 0.1◦ for display. The largest splitting times of $\geq$ 1.4 s are found in the vicinity of the Rio Grande Rift and in the area covered by transitional crust. A closer examination of the spatial distribution of the splitting times (Figure 1.21) suggests that the area with the largest δt values has a coastline that is parallel to the APM. The δt values reduce to about 1.0, s which is the average of of entire study area, near the western extreme of the area covered by transitional crust, where the coastline of the Gulf of Mexico becomes N-S.

The continental interior is characterized by small splitting times of 0.7- 0.9s. The smallest values are located along the suture zone separating the Yavapai and Mazatzal provinces. Interestingly, this is approximately the same area with the largest deviations between the fast directions and APM (Figure 1.20).

4. Discussion

4.1. Stratification of seismic anisotropy

Azimuthal variations of splitting parameters with a $\pi/2$ periodicity is a diagnostic of double-layer anisotropy with horizontal axis of symmetry (Silver and Savage, 1994). We visually examined splitting parameters for all the 547 stations and found that only 13 of them (see Figure 1.21 for their locations) show systematic azimuthal variations. They are located in the vicinity of the Llano Uplift, which is a Precambrian basement uplift in north-central Texas (Mosher, 1998). Figures 1.7b and 1.7c show examples of XKS data recorded by the same station. Significantly different shear-wave splitting parameters were obtained from the two events, which have different back-azimuths. We next attempt to grid-search the 2 pairs of splitting parameters that fit the observed data the best, using the approach 269 presented in Silver and Savage (1994). Because there are normally more than one group of splitting parameters that can fit the data equally well (Gao and Liu, 2009), we use results from surface-wave inversion (Yuan and Romanowicz, 2010) as a priori constraints.

In our study area Yuan and Romanowicz (2010) reported a double-layer anisotropic structure. The top layer, which resides in the lithosphere and is about 150-250 km thick, has an approximately N-S fast direction and a weak anisotropy of about 1.5%. This layer can result in a splitting time of about 0.6-0.8 s for a nearly vertically propagating XKS wave. The bottom layer has an APM-parallel fast direction (about 70◦) and a stronger anisotropy of about 2.5% in most part of our study area. Assuming a thickness of 200 km, the corresponding splitting time is about 1 s.

The blue lines in Figure 1.22 were computed using the above splitting parameters derived from surface wave inversion results (0◦ and 0.75 s for the top layer, and 70◦ and 1.0 s for the lower layer), by assuming a XKS frequency of 0.2 Hz. Although the misfits are obvious, the general trends of the computed lines follow those of the observed data closely, especially for the fast directions. To obtain a better fit, we search the optimal set of parameters in vicinity of the surface-wave derived fast directions and free-varying splitting times, that is, (40◦-90◦, 0.0-2.0 s) for the lower layer, and (-25◦-25◦ , 0.0-2.0 s) for the top layer. The resulting best-fitting parameters are (60◦, 1.3 s) for the lower layer, and (-19◦, 0.4 s) for the top layer. The green lines in Figure 6 are computed using the best-fitting parameters.

On the Llano Uplift and surrounding areas, the azimuthal variations of our SWS parameters and results from the grid-search above are in agreement with the surface-wave inversion results of Yuan and Romanowicz (2010). However, Yuan and Romanowicz (2010) also observed the existence of lithospheric anisotropy with a nearly N-S fast direction in the rest of our study area, and our SWS measurements do not show systematic azimuthal variations except for the 13 stations in the vicinity of the Plateau. One of the possible causes for the discrepancy could be the large difference in the frequency bands of the seismic waves used by the two types of studies.

Surface waves have much longer period and thus are capable of detecting long-wave features. Small-scale (relative to the wavelength) heterogeneities in anisotropic properties in the lithosphere are smoothed out. On the other hand, XKS waves have

shorter wavelength and consequently such heterogeneities can have a significant impact on the results. If the heterogeneities are strong enough in the form of multiple layers and/or dipping axis of symmetry, the effect of anisotropy as observed by XKS waves can be canceled out. The fact that stations on the Llano Uplift show clear two-layer anisotropy suggests a relatively homogeneous anisotropic structure in the lithosphere beneath this area.

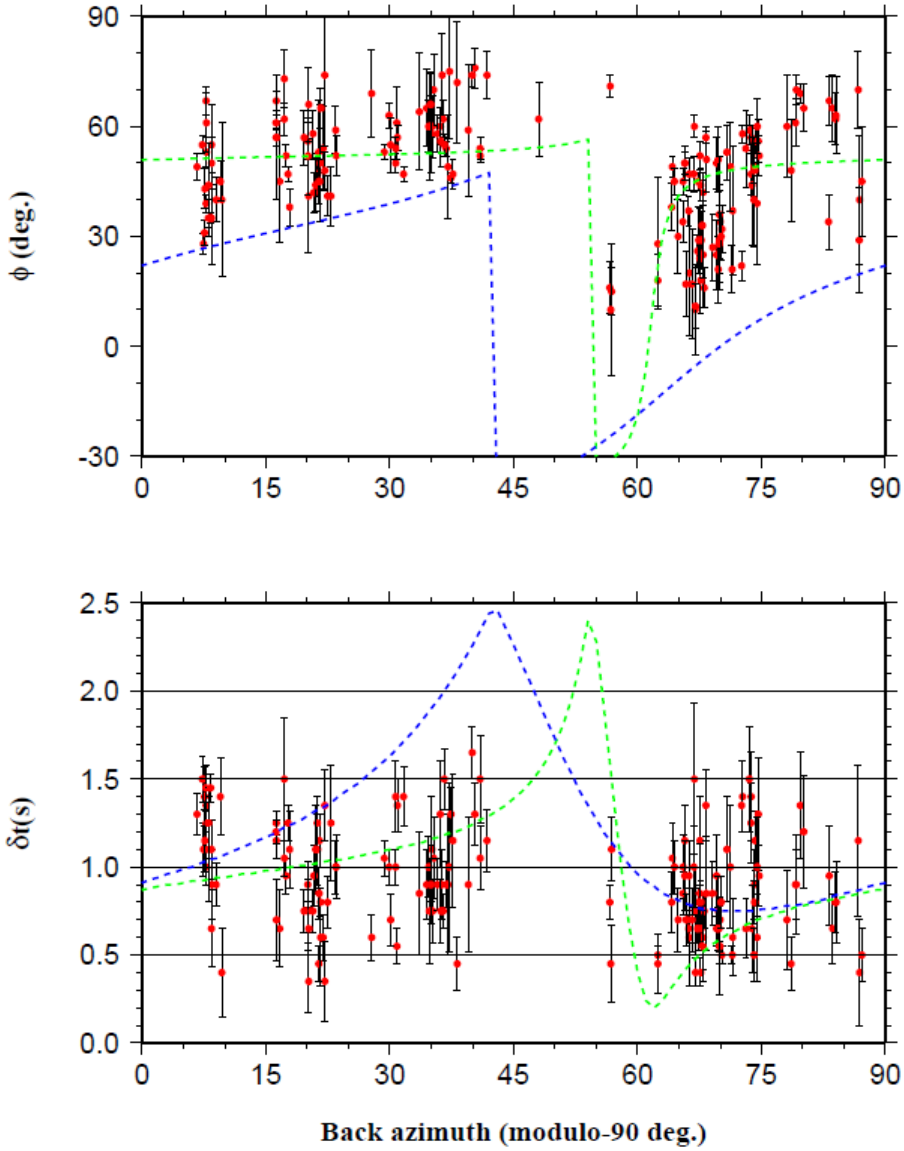

Figure 1.22. Azimuthal variations of fast directions (top plot) and splitting times (bottom plot) for the 13 stations shown in Figure 1.21. The green lines were computed using the optimal splitting parameters from grid-searching under a two-layer model, and the blue lines were computed using approximate splitting parameters estimated based on inversion of surface waveforms (Yuan and Romanowicz, 2010).

4.2. Estimating the depth of anisotropy beneath the study area

Previous studies revealed that the fast polarization directions are mostly parallel to the APM direction or align with the strike of the geological features (Silver and Chan, 1991; Silver, 1996). Thus the observed seismic anisotropy using SWS either represents lithospheric or asthenospheric origin or a combination of the two (Long and Silver, 2009; Savage, 1999). If the fast polarization direction is in alignment with the absolute plate motion, the splitting parameters will primarily reflect the asthenosphere source (Conrad et al., 2007). The plate motion will enhance the mineral to orient, preferably, into the direction of the infinite strain axes. Therefore, the fast polarization directions will be parallel to either the absolute plate motion shear or the mantle flow direction (Karato et al., 2008; Huang et al., 2011).

Conversely, if the anisotropy reflects the lithospheric origin, the shear wave splitting observation would be expected to be parallel to the surface geological features (Nicolas and Christensen, 1987; Nicolas, 1993; Savage, 1999; Silver, 1996). Mountain belts, major faults, and extensional rifts including continental margins are good examples in which anisotropy will reside in the lithospheric mantle (Silver, 1996). Thus the key information to distinguish between lithosphere or asthenosphere origin of observed anisotropy is a reliable determination of the depth of the source of anisotropy.

Determination of the anisotropy location is still a topic of argument in shear wave splitting studies. The source of anisotropy can occur anywhere at any anisotropic layer from the core-mantle boundary to the recording station at the surface (Gao et al., 2010; Barruol and Hoffmann, 1999).

In this study we use the spatial variation factor approach (Gao et al., 2010; Liu and Gao, 2011) to estimate the depth of anisotropy. A detailed description of the approach (and an accompanying freely-accessible FORTRAN program) can be found in Gao and Liu (2012), and is briefly summarized below. The procedure is built upon the principle that for a given XKS ray path traveled through an interface, the distance between the recording station and the surface projection of the ray-piercing point at the interface increases for deeper interface. When multiple events from various azimuths are recorded by closely-spaced stations, the splitting parameters observed on the surface reach the highest spatial coherency if the interface is placed 344 at the true depth.

In practice, the optimal depth is searched by assuming a series of depth from 0 to 400 km at an interval of 5 km. The spatial variation factor as defined in Liu and Gao (2011), Fv, is computed for each of the assumed depths:

$$F_v = \frac{1}{N}\sum_{i=1}^{N}\sqrt{\frac{1}{M_i - 1}}\left(w_\phi \sqrt{\sum_{j=1}^{M_i}\left(\phi_{ij} - \overline{\phi_i}\right)^2} + w_{\delta t}\sqrt{\sum_{j=1}^{M_i}\left(\delta t_{ij} - \overline{\delta t_i}\right)^2} \right)$$

Where N is the number of blocks, M_i is the number of the events in each block, and ϕ_{ij}, and δt_{ij} are the fast direction and the time delay respectively. The resulting Fv curves for the 4 areas are shown in Figure 1.23. Beneath the western US orogenic zone and the area covered by transitional crust, the depth-estimate procedure found that the main contribution to the observed anisotropy is originated from a depth of about 150 km, and beneath the Great Plains, it is in the range of 200-250 km. These values remarkably agree with the thickness of the lithosphere beneath the respective areas estimated using various seismic techniques (van der Lee and Nolet, 1997; Wilson et al., 2005; Yuan and

Romanowicz, 2010; Burdick et al., 2012). Such agreements suggest that the observed anisotropy mostly come from the top of the asthenosphere.

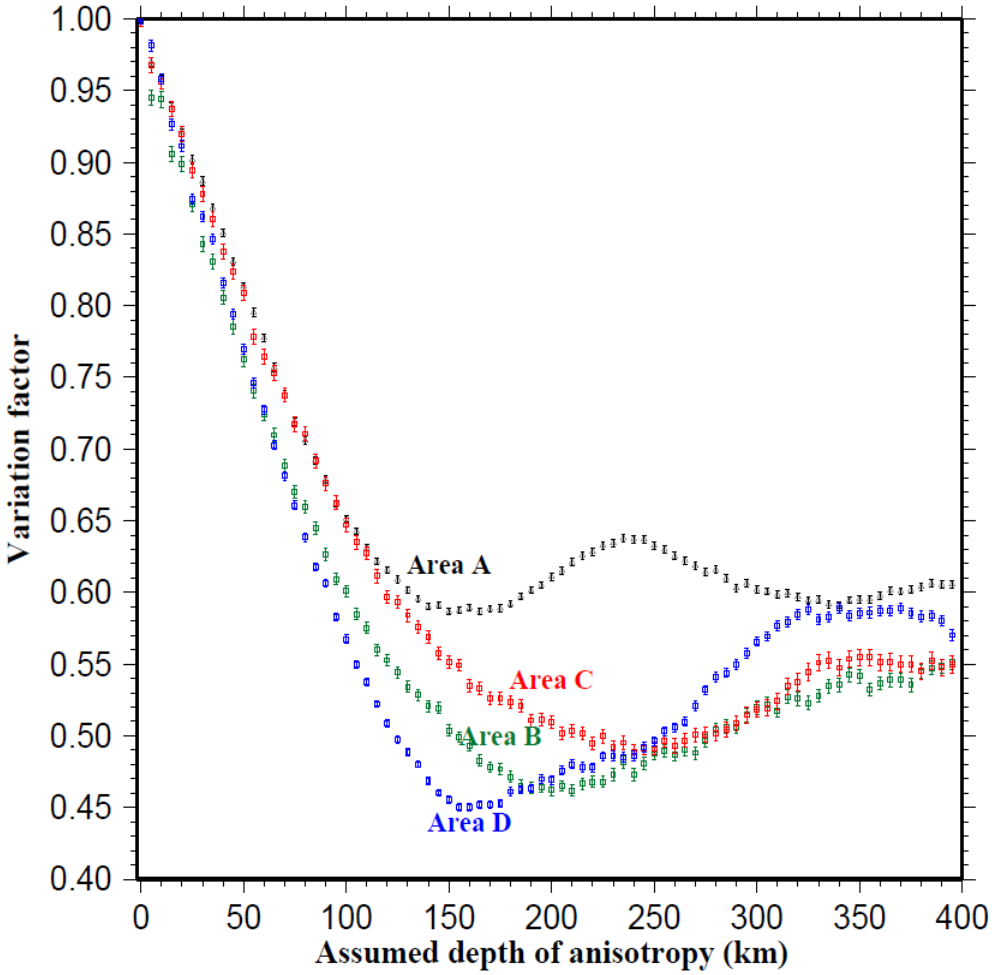

Figure 1.23. Spatial variation factors as a function of assumed depth of the source of anisotropy for each of the four areas.

4.3. Locating the edge of the North American craton

As discussed below, the observed anisotropy patterns are largely controlled by the edge of the North American craton. To obtain a first-order estimate of the shape of the cratonic edge, we obtained and processed data from all the USArray TA stations in the study area, from teleseismic earthquakes (in the epicentral distance range of $30^\circ - 180^\circ$). The cutoff magnitude used for data requests is a function of focal depth and epicentral distance, as described in Liu and Gao (2010). The cut-off magnitude is determined using $M_c = 5.2 + (D_e - 30.0)/(180.0 - 30.0) - H_f/700$, where D_e is the epicentral distance in degree, and H_f is the focal depth in km. The vertical components are then filtered in the frequency band of $0.04 - 1.0$ Hz. An automatic trace-selection procedure is applied to the filtered seismograms to select those with a strong first arrival.

The procedure utilizes the ratio between the absolute maximum value in the signal window and the mean absolute value of a noise window before the first arrival. Those selected for further processing have a ratio of 4.0 or greater. For a given event, the waveform cross-correlation approach (VanDecar and Crosson, 1990) was used to pick the relative travel-time residual at each station, and the residuals for all the events at each station are averaged to obtain a mean residual for each of the stations. The results shown in Figure 1.24 were obtained by smoothing the station averages in 1° by 1° windows and by resampling to a finer resolution of 0.1°. The travel-time residuals of the first P-wave (including P, P_{diff} and PKP) show systematic spatial variations.

The peak-to-peak amplitude in the study area is about 2.0 s. Most part of the Rio Grande Rift has a positive anomaly of about 0.5 s, and the area covered by transitional

crust is characterized by overwhelmingly positive residuals of as large as 1.5 s. While the thick sedimentary cover in the extended areas contributes to the observed positive anomalies, calculations using reasonable assumptions of thickness and velocity anomalies of the sedimentary cover suggest that a significant amount of the travel-time delays must come from the mantle, most likely as a result of a thinner lithosphere relative to the continental interior. Seismic tomography studies suggest that the edges of cratons have a cone shape, dipping toward the interior at greater depth (Burdick et al., 2012; James et al., 2001).

Therefore, there is no single definition of the edge that can represent the entire lithosphere. If we use the contour line of 0.25 s, which is the average residual in the study area, to approximately represent the edge of the lithosphere, the eastern boundary of the Rio Grande Rift and the northern boundary of the area with transitional crust are almost consistent with the cratonic edge. Note that under this definition, the south western corner of the craton extends beyond the US-Mexican border, into an area that has not been sufficiently covered by seismic stations (Figure 1.24). This is consistent with results from a recent P-wave tomography study using USArray data (Burdick et al., 2012).

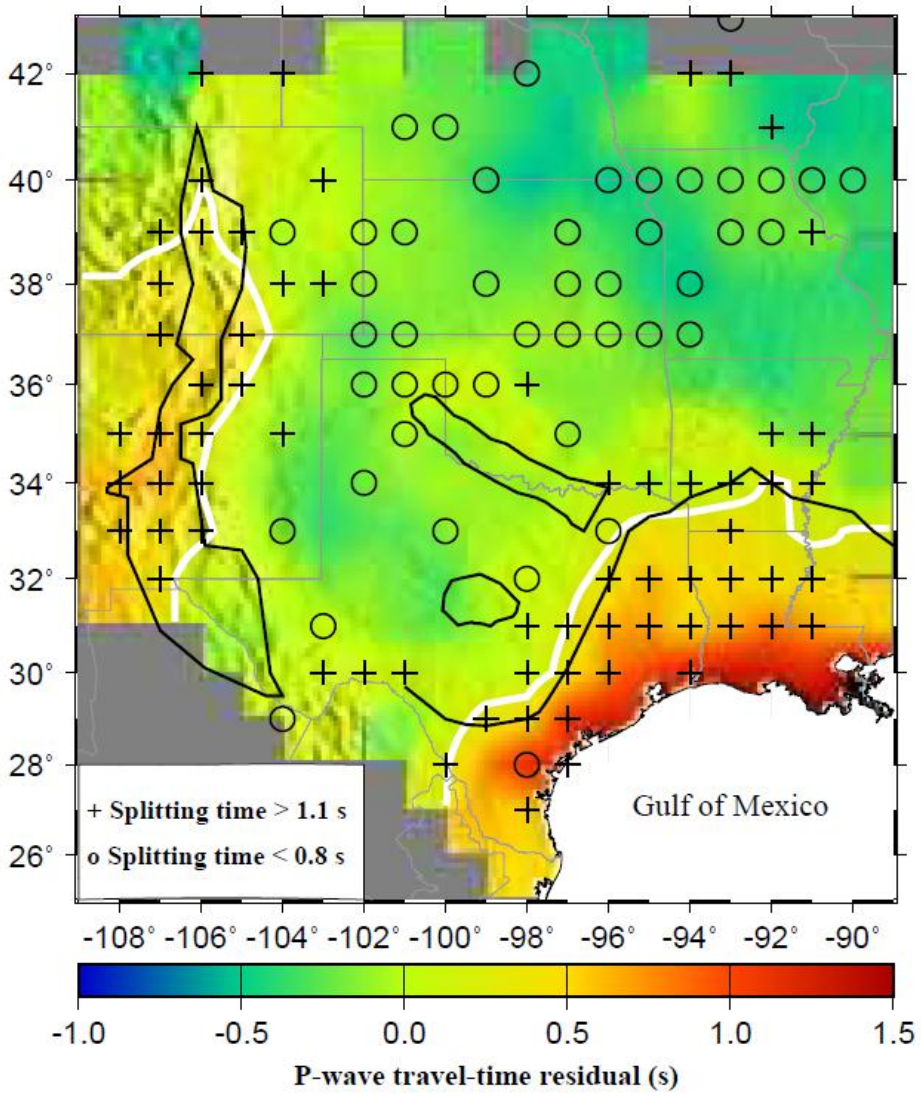

Figure1.24. Spatial correspondence between shear-wave splitting times and teleseismic P-wave travel-time residuals. The largest splitting times (pluses) are found along the margins of the North American craton, while the smallest values (circles) mostly locate in the interior of the craton.

4.4. Argument against significant lithospheric contributions to observed anisotropy

On the lithospheric scale, two anisotropy-forming mechanisms have been proposed (Silver, 1996). The first is LPO of olivine a-axis under uniaxial compression which leads to a fast direction that is perpendicular to the shortening direction, and the other is the presence of vertical magmatic dikes which result in dike-parallel fast directions. Based on a limited number of SWS measurements, some previous studies (Silver and Chan, 1988; Silver, 1996; Barruol et al., 1997; Gao et al., 2008) proposed a lithospheric origin for the observed anisotropy beneath the North American craton. As argued below, neither mechanism seems to be the dominant cause of the observed XKS anisotropy beneath the study area.

Although the parallelism between the APM and most portions of the Proterozoic sutures makes it difficult to distinguish the contributions from the lithosphere and asthenosphere, several lines of evidence suggest that collisional orogenies associated with the suture zones did not create significant vertically coherent deformation in the lithosphere, for the following reasons:

1).The suture zones are not associated with zones of large splitting times. Because the maximum compressional strain is expected to be found along the suture zones, if such strain is responsible for observed anisotropy, the splitting times in the vicinity of the suture zones should be greater than those in the interior of the Proterozoic provinces. This is not observed for either suture zones (Figure 1.21).

On the contrary, the smallest splitting times in the entire study area are found in the vicinity of the Yavapai-Mazatzal suture (Figure 1.21). 2). the fast directions do not

follow the strike of the suture zones. Most part of the Mazatzal-Grenville suture is not parallel to the APM (Figure 1.20). Instead, its strike varies significantly. Such variations are not consistent with the fast directions in the vicinity of the zone, which are dominantly parallel to the APM. Most of the fast directions in the vicinity of the Yavapai-Mazatzal suture also show a significant angle with the strike of the zone (Figure 1.20). 3). Both suture zones extend westward to the western US orogenic zone with a NE-SW or NNE-SSW strike (Figure 1.1), but the fast directions in the orogenic zone and its transition with the Great Plains are mostly N-S. 4). the splitting times do not increase with increased thickness of the lithosphere.

Under the assumption of constant lithospheric anisotropy in the study area, areas with thicker lithosphere should correspond to greater splitting times. Such a positive correlation is not observed. In contrast, the largest observed splitting times are found beneath areas with extended crust on the western and southern margins of the craton, and the smallest splitting times are located in the continental interior where the lithosphere is the thickest (Figure 1.24). Due to chemical or thermal (for recent dikes) contrasts with surrounding rocks, vertical or near-vertical dikes in the lithosphere especially those associated with continental rifting and formation of passive margins can produce mechanical anisotropy. This mechanism was proposed as a possible cause for the observed seismic azimuthal anisotropy in the Baikal and East African rift zones (Gao et al., 1997; Kendall et al., 2005) and the north margin of the Gulf of Mexico (Gao et al., 2008). The dikes are expected to be parallel to the rifts or margins. While such dikes can explain the N-S oriented fast directions in the northern half of the Rio Grande Rift, which

has a N-S strike, they are unlikely to be responsible for those observed on the southern half of the rift, because the strike of the rift turns southwestward but the fast directions remain N-S (Figure 1.20). In addition, N-S fast directions are observed across a wide zone of several hundred km away from the rift axis, and it is thus unlikely that rift-parallel lithospheric dikes can extend this far (Figure 4). The fast directions observed on the transitional crust north of the Gulf of Mexico are parallel to the coastline (Figure 1.20), and thus in principle can be attributed to margin-parallel dikes.

However, as evidenced by gravity and magnetic data (Mickus et al., 2009), the western margin of the Gulf of Mexico is equally magmatic, and the associated dikes are mostly to be oriented parallel to the coastline, which is N-S oriented. The observed fast directions in this area are mostly NE-SW (Figure 1.20) and thus are not consistent with a dike origin. The above arguments, plus the results of depth estimate using spatial coherency of SWS parameters (Figure 1.23), exclude an overall lithospheric origin of the observed anisotropy. But they do not exclude observable lithospheric contributions for some of the areas. One such area is the Llano Uplift. The top layer could be in the lithosphere and could be formed during the Mesozoic when the Northern American plate was moving toward the north (Yuan and Romanowicz, 2010). Some NW-SE oriented fast directions in the vicinity of the Southern Oklahoma aulacogen could also reflect fabrics in the lithosphere.

4.5. Asthenospheric origin of anisotropy: A preliminary model

The evidence presented above for the lack of significant lithospheric contribution to the observed anisotropy, especially the results of depth estimate using spatial coherency of splitting parameters (Figure 1.23), suggests that most of the observed anisotropy has an origin in the upper asthenosphere. The anisotropic layer corresponding to the observed splitting times has a thickness of about 100 km, which is inconsistent with the existence of an ultra-thin, low viscosity layer at the base of the lithosphere. Such APM-parallel anisotropy in the upper asthenosphere is indicative of a certain degree of lithosphere-asthenosphere coupling (Marone and Romanowicz, 2007). Numerical modeling suggests that large viscosity difference of 8-10 orders of magnitude can lead to decoupling between the lithosphere and asthenosphere (Doglioni et al., 2011). Therefore the observed anisotropy suggests a relatively small viscosity difference between the two layers.

Seismic anisotropy as revealed by SWS and surface waveform inversion, however, cannot unambiguously determine the sense of relative motion between the two layers, i.e., both a faster lithosphere and a faster asthenosphere can lead to the same or similar patterns of anisotropy, under reasonable assumptions of mantle velocity, viscosity, and other physical parameters. For instance, finite difference modeling of mantle flow around cratonic keel leads to an identical flow pattern at the up and down stream sides of the craton (Fouch et al., 2000). Thus other constraints, such as additional geodynamic modeling effort (e.g., Bird et al., 2008) that utilizes the new SWS data set presented here, are required to distinguish the two models. Because the two models imply the opposite (resistive or active driving) effects of the asthenosphere on plate motion,

such [4]efforts are important to understand plate dynamics. Since both models can explain all the major characteristics of the spatial variations of the observed splitting parameters, in the following, we apply faster-moving lithosphere model (Figure 1.25) to explain the observations.

They can be explained equally well by reversing the direction of the flow, i.e., a mantle flow moving around the keel of the craton (Fouch et al., 2000), and APM-parallel shear strain in the continental interior. The faster-moving lithosphere model suggests that beneath the western US orogenic zone and its transitional area with the Great Plains, the southwestward moving continental root dispatches asthenospheric flow along its edge (Figure 1.25). The flow moves southward and forms N-S oriented seismic anisotropy. This flow system turns eastward around the southwest corner of the root, which is beneath northern Mexico, as suggested by the nearly E-W fast directions approximately at (103°W, 29.5° N). The strength of the flow reaches its maximum beneath the area covered by transitional crust north of the Gulf of Mexico, probably because the lithosphere beneath this area has an edge that is more vertical than other areas, and consequently the flow is concentrated in a narrower zone. The APM-parallel anisotropy beneath the continental interior can be attributed to simple shear strain originated from the relative movement between the base of the lithosphere and a layer with a thickness of about 100 km at the top of the asthenosphere.

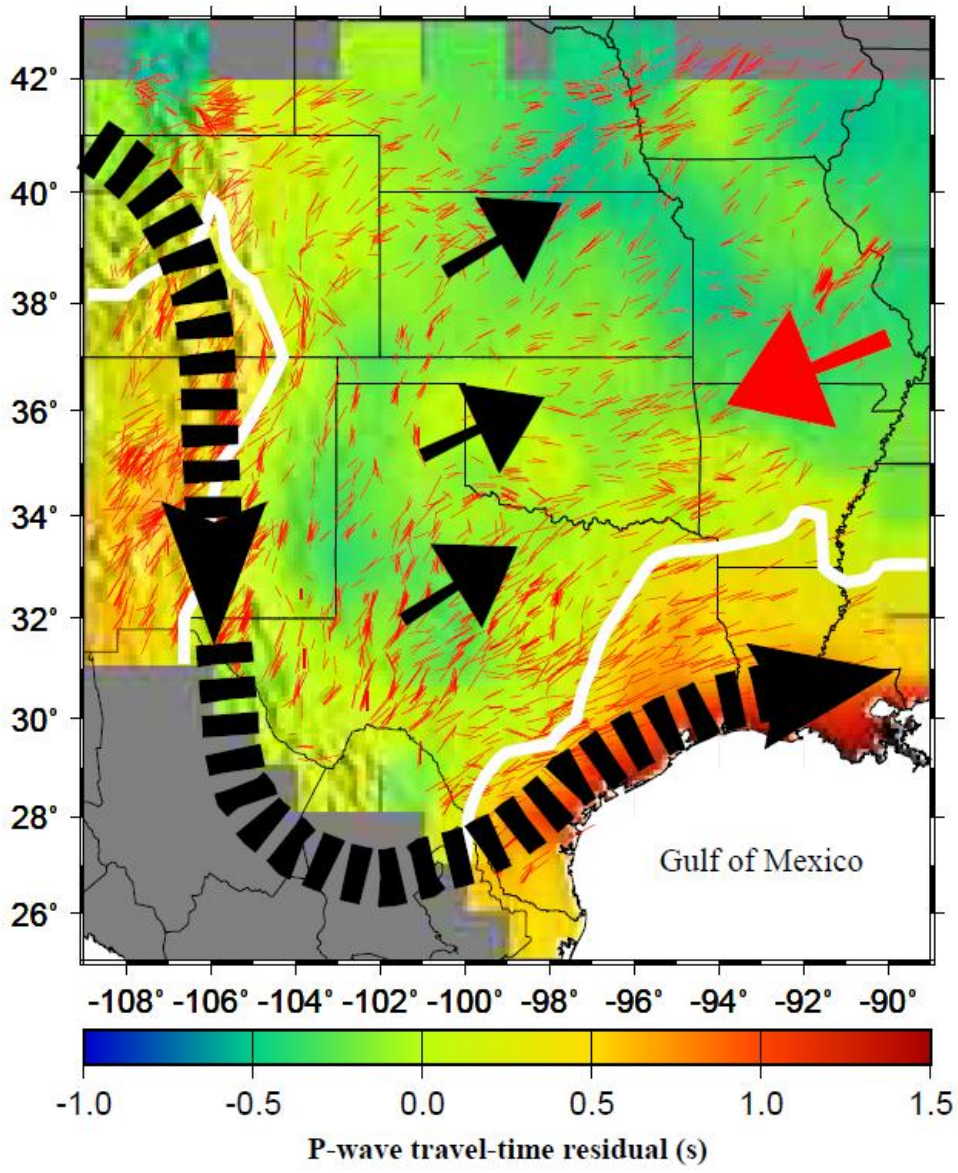

Figure 1.25. Schematic diagram showing direction of flow lines in the asthenosphere under the assumption of a faster-moving lithosphere relative to the asthenosphere. The solid black arrows indicate shear-strain in the asthenosphere beneath the craton, and the thick dashed line represents flow around the edge of the North American craton. The directions are relative to the underlying asthenosphere. The red arrow shows the APM direction of the North American plate, and the thin red bars represent individual shear-wave splitting measurements (Figure 1.20). The background image shows P-wave travel-time residuals, and the white lines indicate the approximate edge of the craton. Note that for the alternative faster-moving asthenosphere model, the direction of the black arrows are reversed.

5. Conclusions

Systematic spatial and azimuthal variations of shear-wave splitting parameters are observed beneath the southwestern edge of the North American craton and adjacent areas. Spatial coherency analysis of the splitting parameters suggests that the observed anisotropy 518 is mostly from the upper asthenosphere, implying a certain degree of coupling between the lithosphere and the asthenosphere. The systematic variations and the depth distribution of the source of anisotropy can be adequately interpreted by the southwestward movement of the lithosphere over a slower moving or stagnant asthenosphere. The root of the continent dispatches mantle flow to form strong anisotropy with LPO of olivine a-axis parallel to the edge of the continent. In addition, beneath the continental interior, shear-strain in the top layer of the asthenosphere from the movement of the lithosphere is the most likely source of APM-parallel anisotropy.

Teleseismic P-wave travel time residuals indicate that the southwestern extreme of the North American craton is located in northern Mexico, an area that has not been investigated using broadband seismic data. A seismic experiment with USArray-comparable station density in this area is needed to locate the edge and image the mantle structure. Those results, when combined with results from geodynamic modeling, are essential to test various models regarding continental structure and dynamics, including the mantle flow models presented in this study.

Acknowledgments

Data used in the study were obtained from the IRIS DMC. This study was supported by the US National Science Foundation grants EAR-0952064 and EAR-1009946 to K.L. and S.G.

APPENDIX

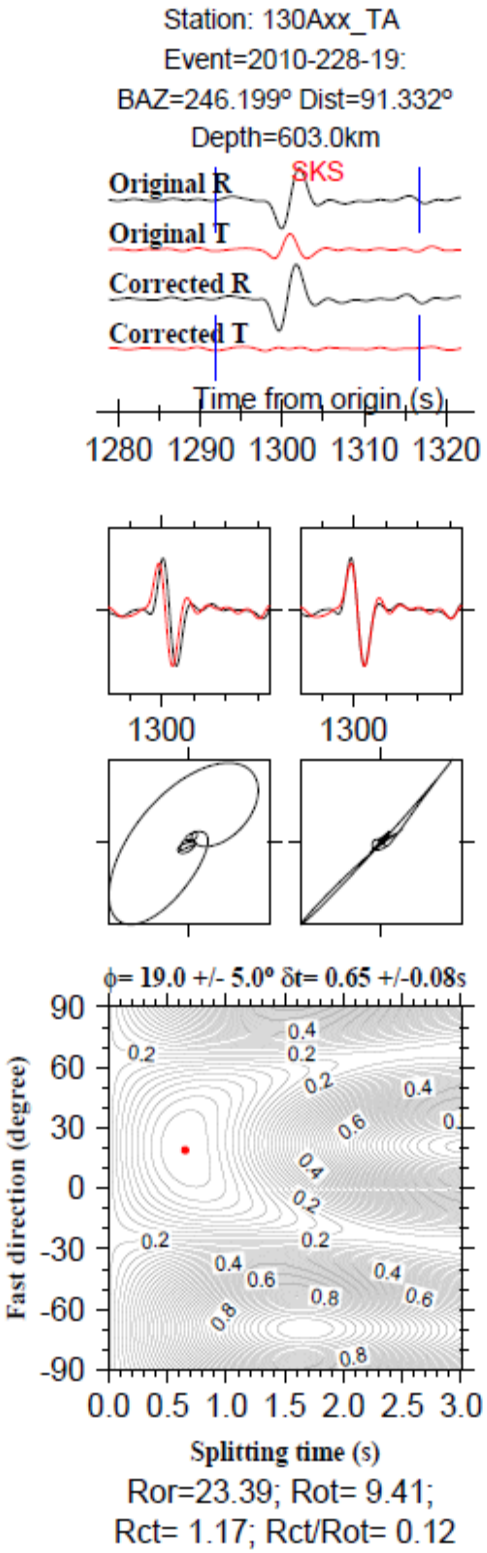

C1. An example of SKS quality **A** for station 130A.

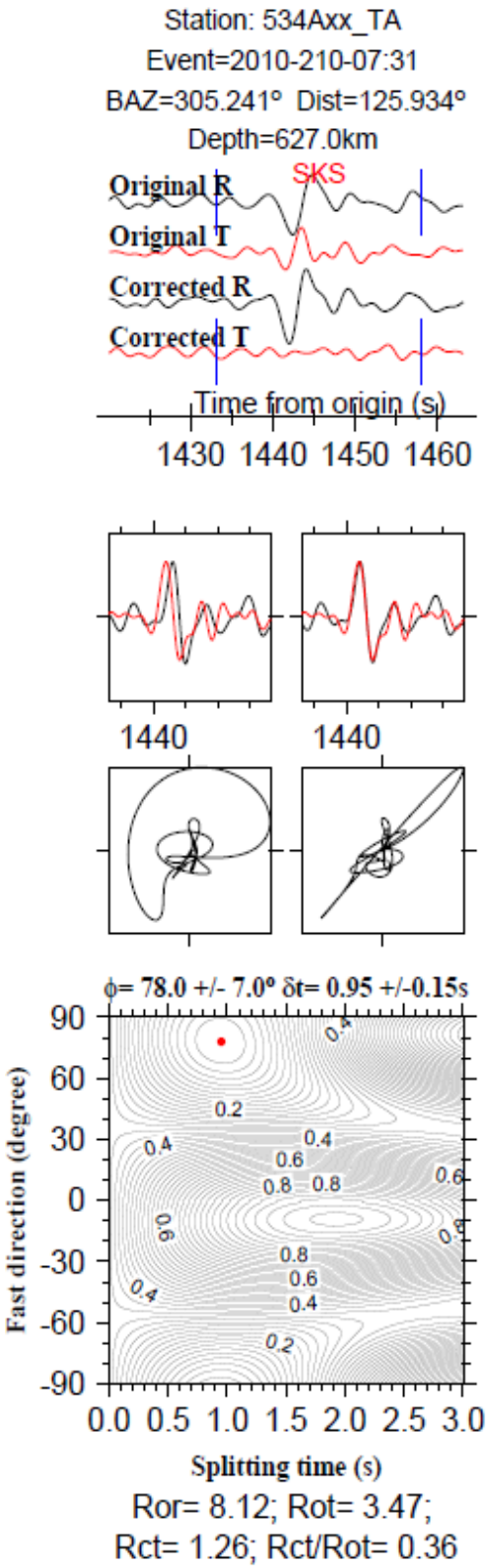

C2. An example of SKS quality **B** for station 534A

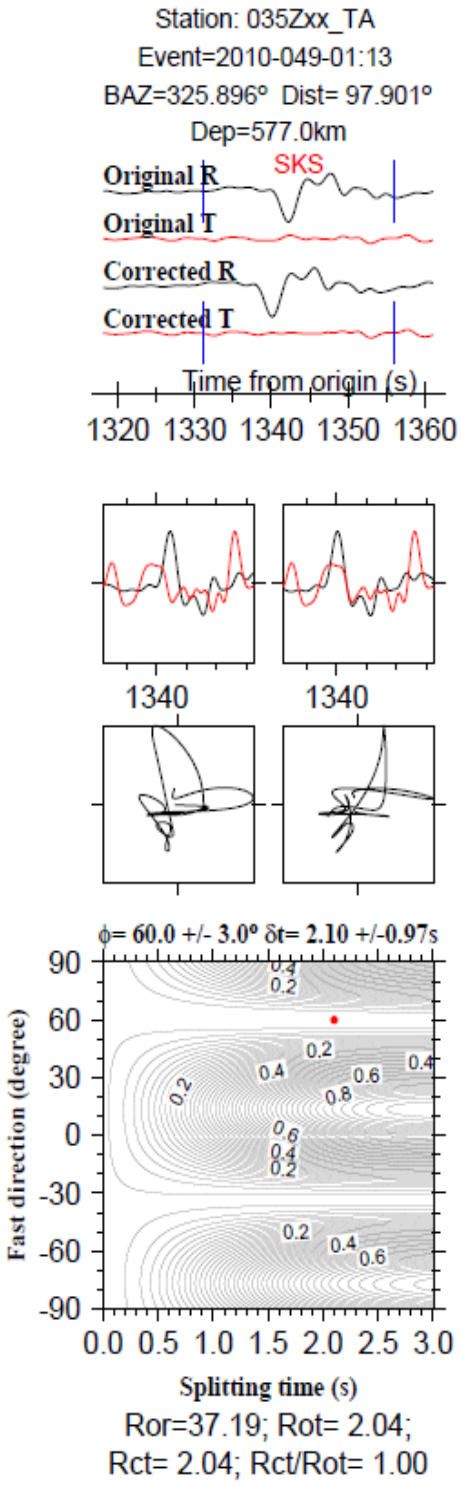

C3. An example of SKS quality **N** for station O35Z

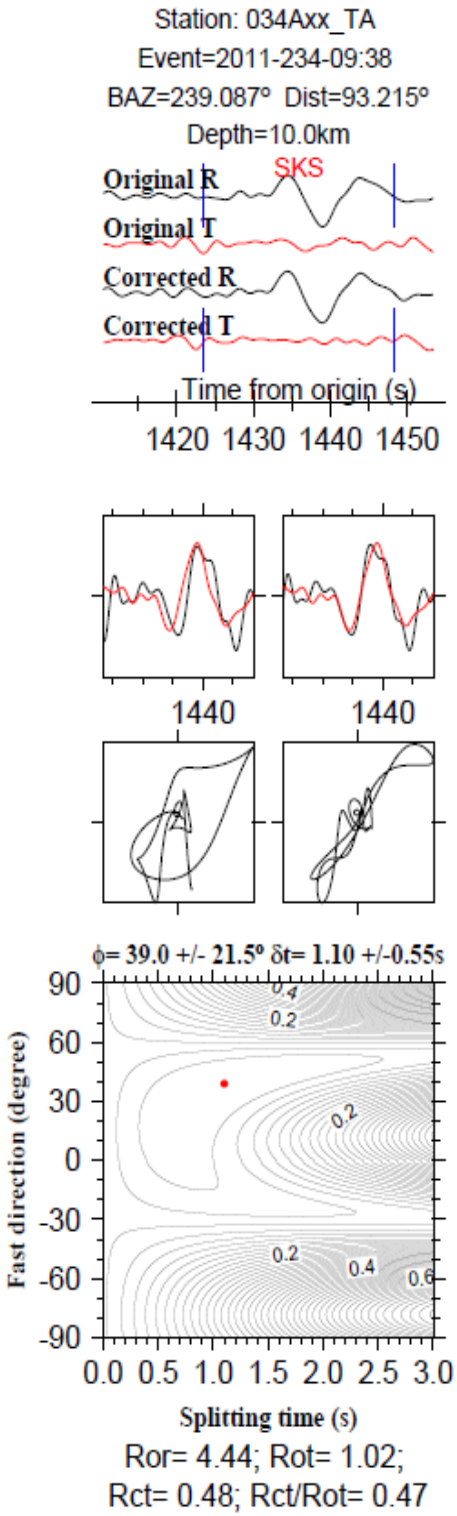

C4. An example of SKS quality **C** for station O34A

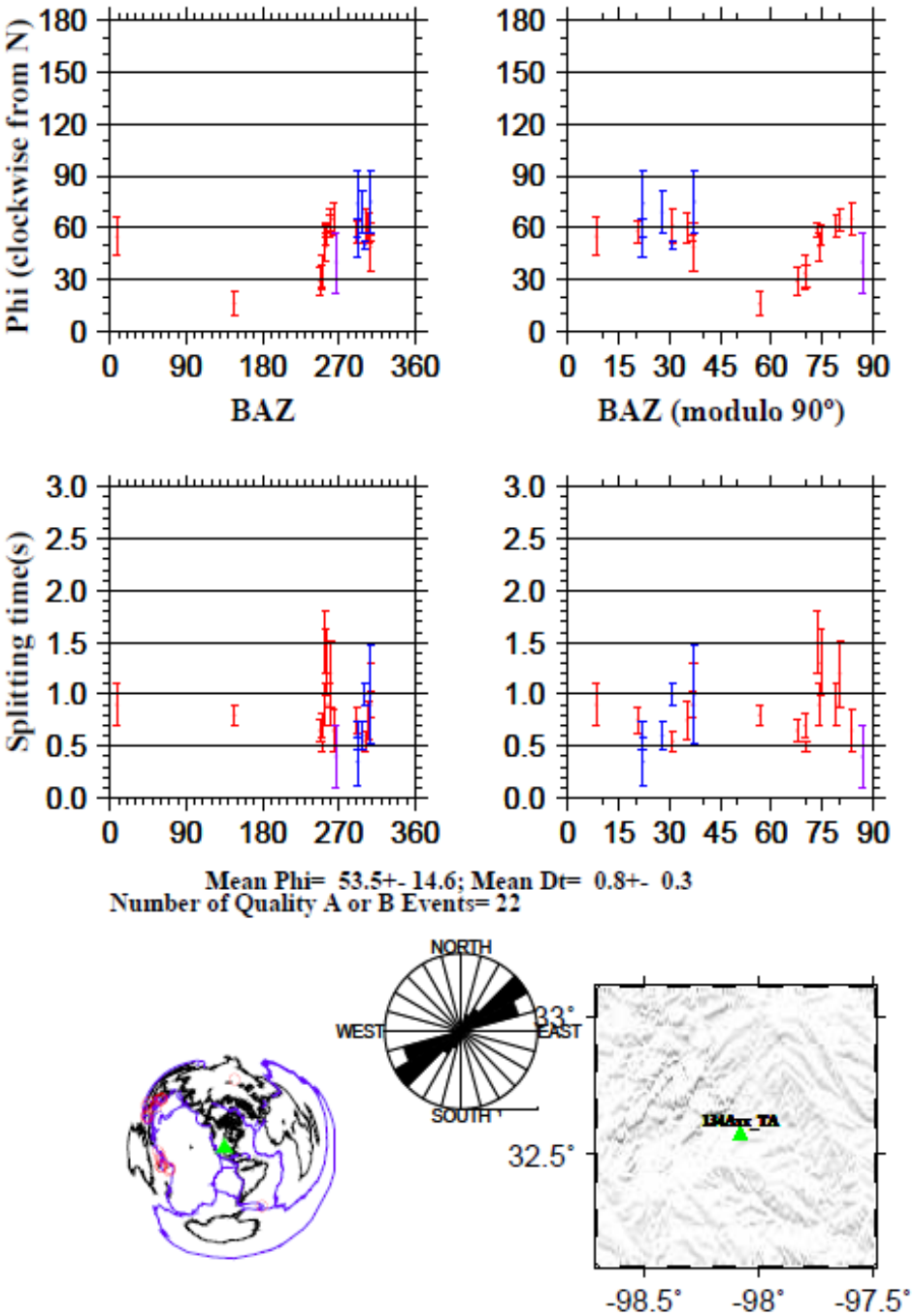

C5. Azimuthal variations of fast direction (top) and the splitting time delay (middle) and the distribution of the events and rose diagram of measurements for TA station 134A demonstrate the presence of two-layer anisotropy.

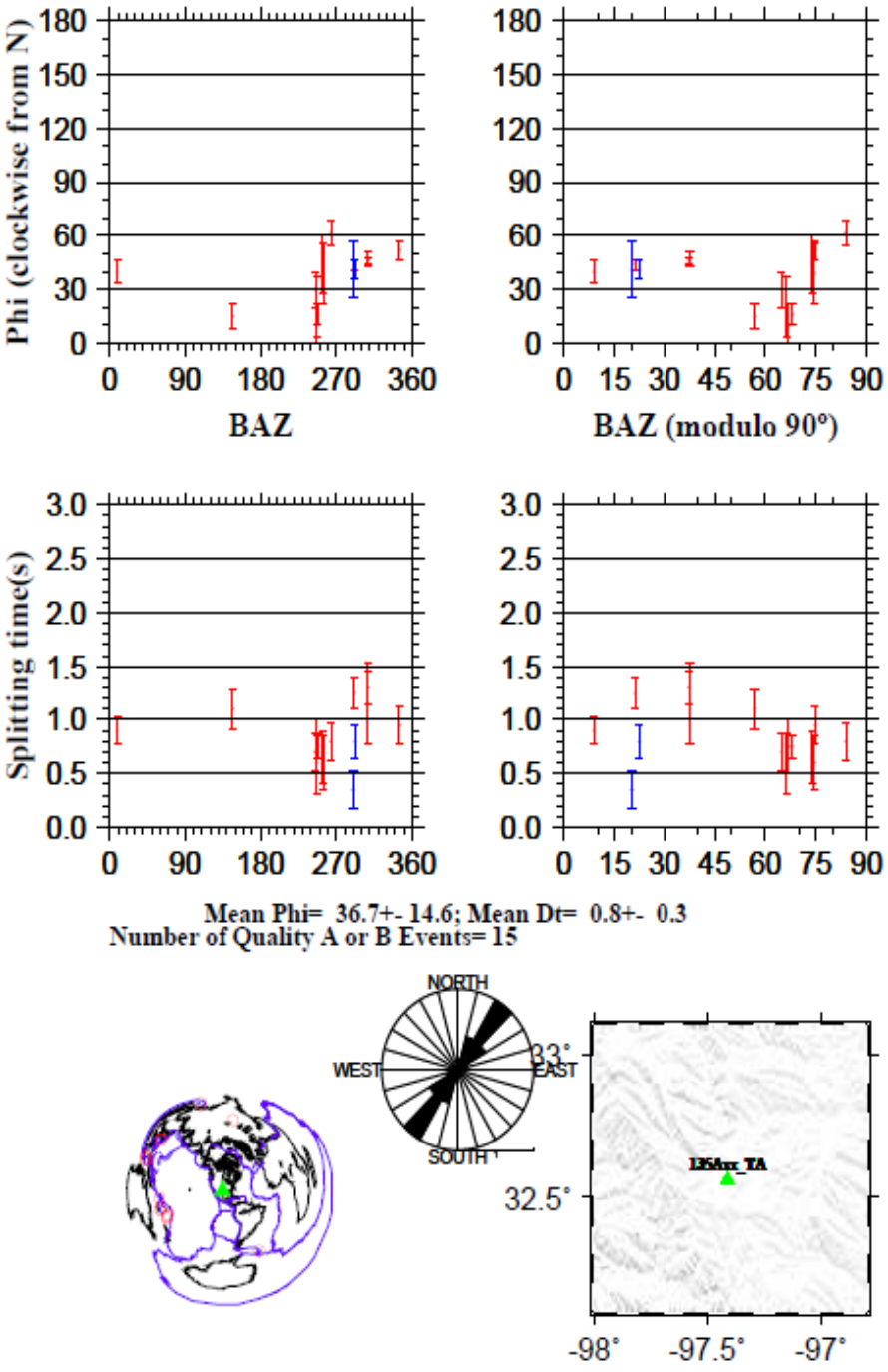

C6. Same as C5, but for station 135A.

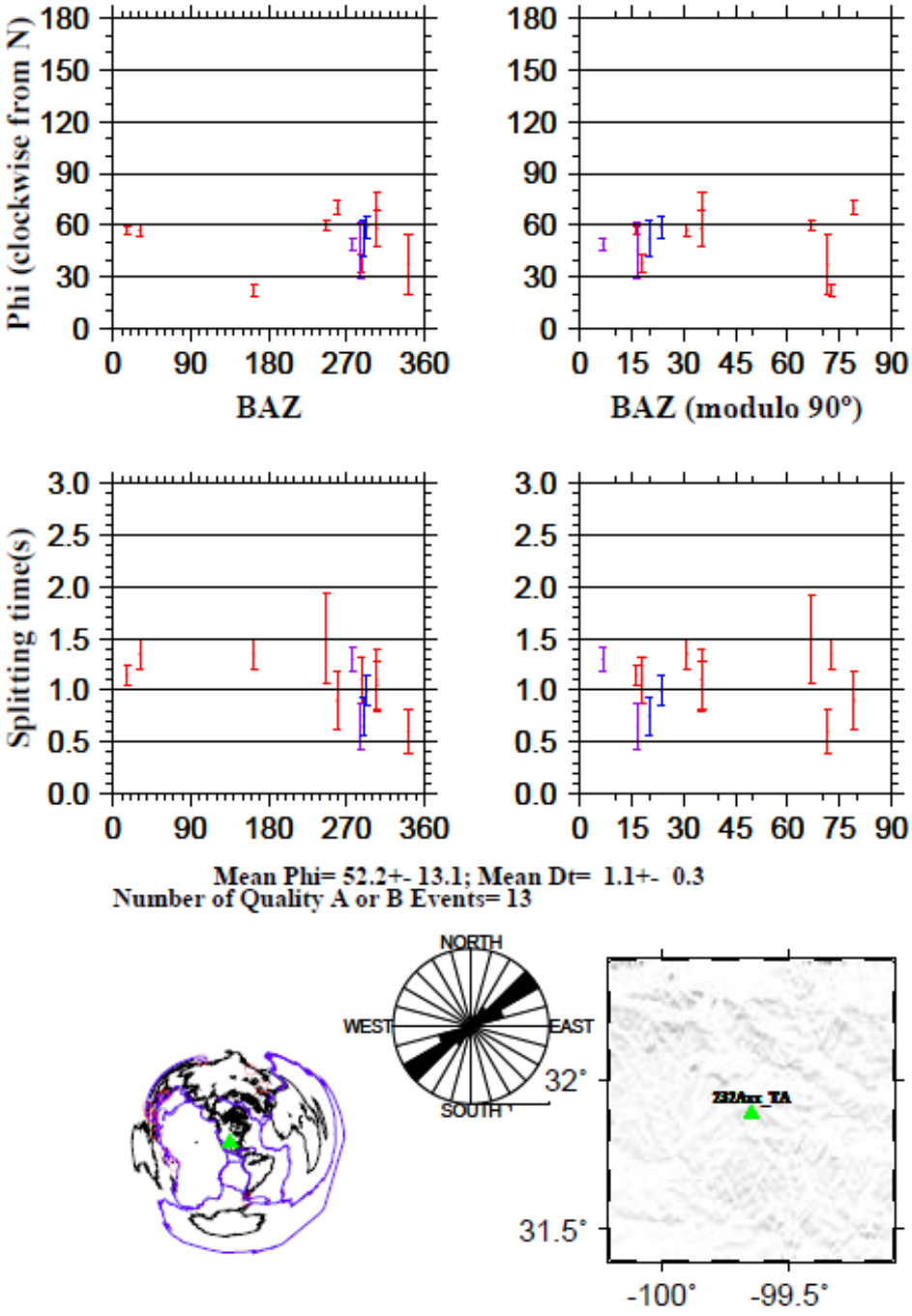

C7. Same as C5 but for station 232A.

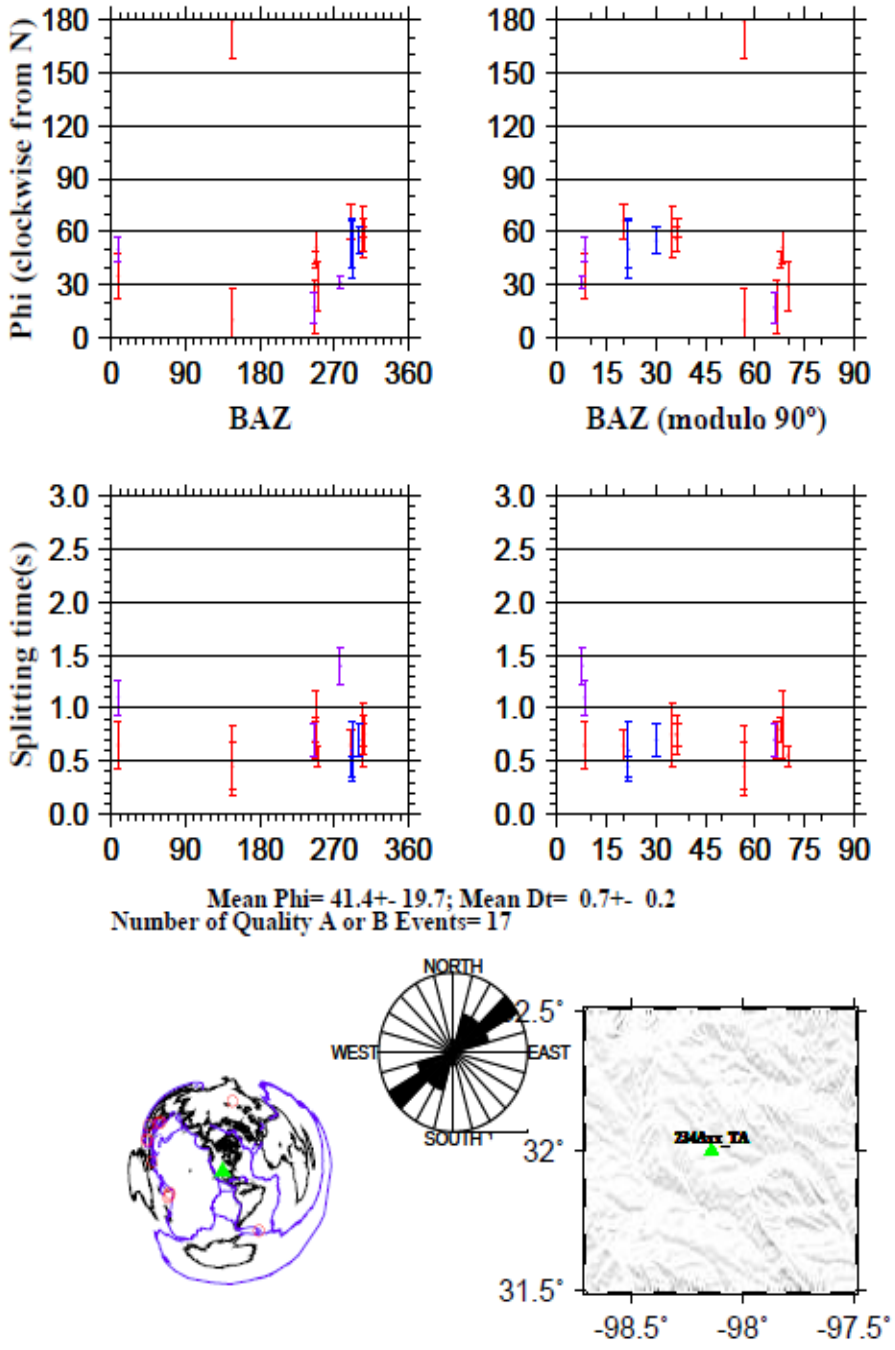

C8. Same as C5, but for station 234A.

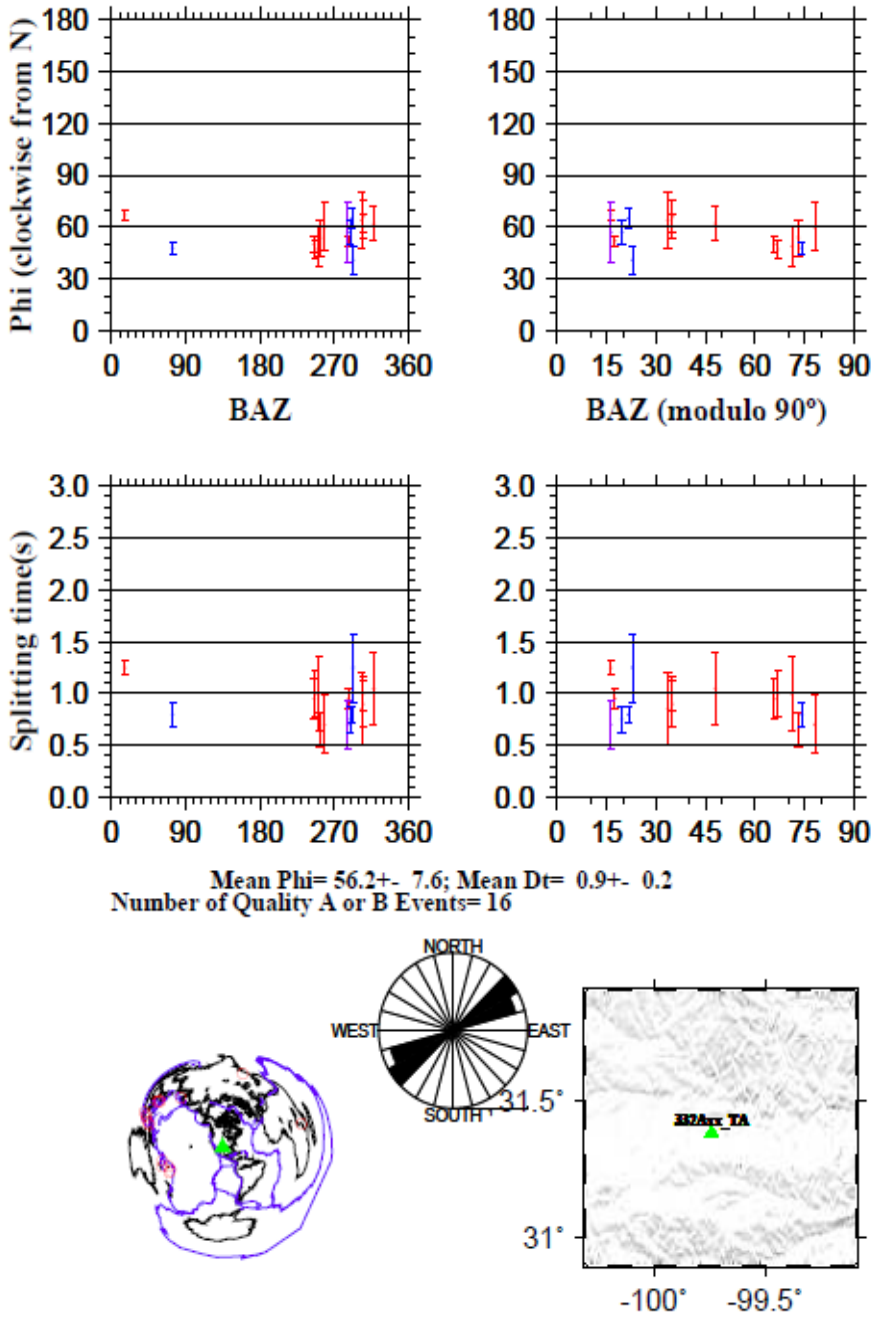

C9. Same as C5, but for station 332A

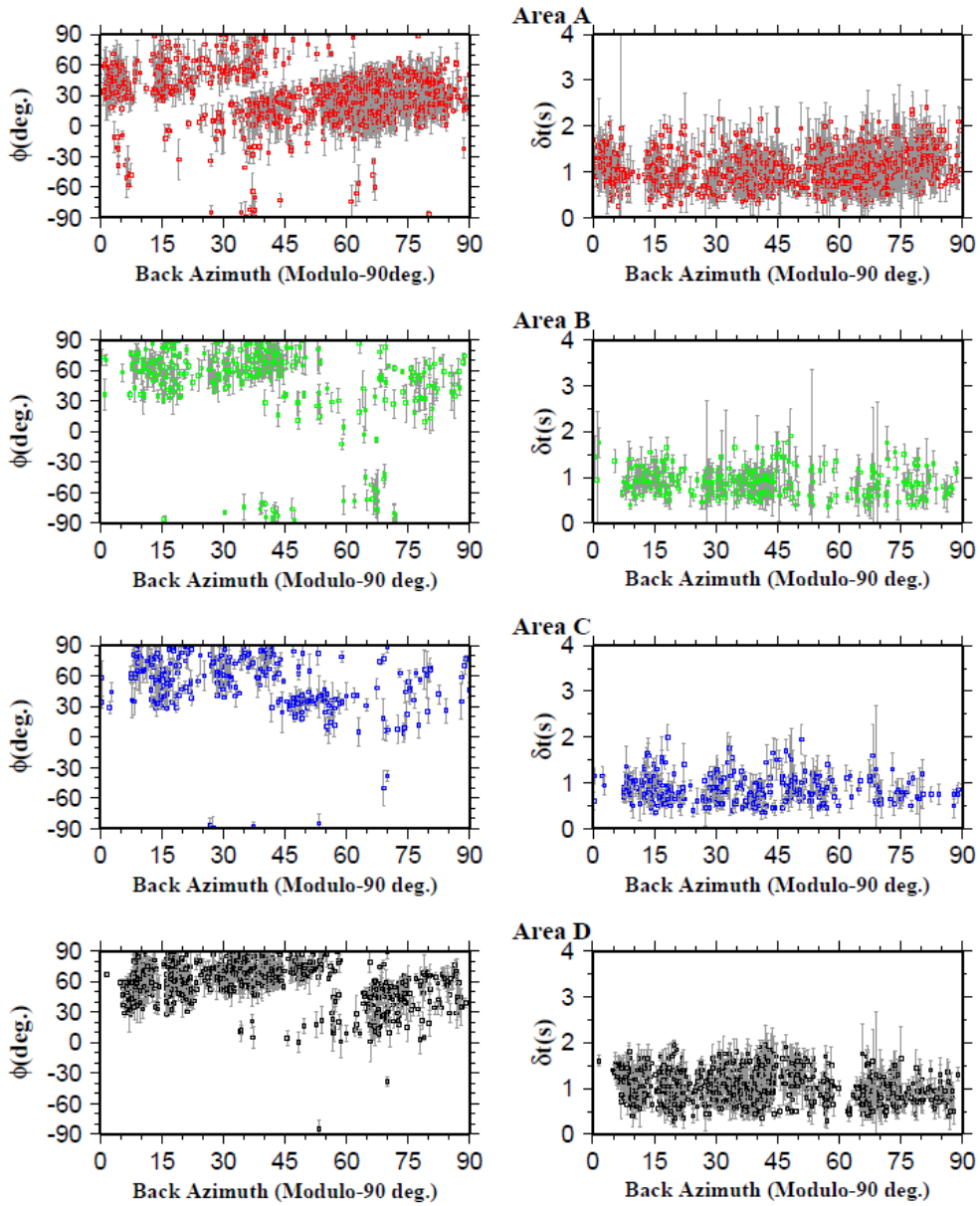

C10. Azimuthal variations of resulting splitting parameters for station on the four subareas (A, B, C, and D) on the area of study.

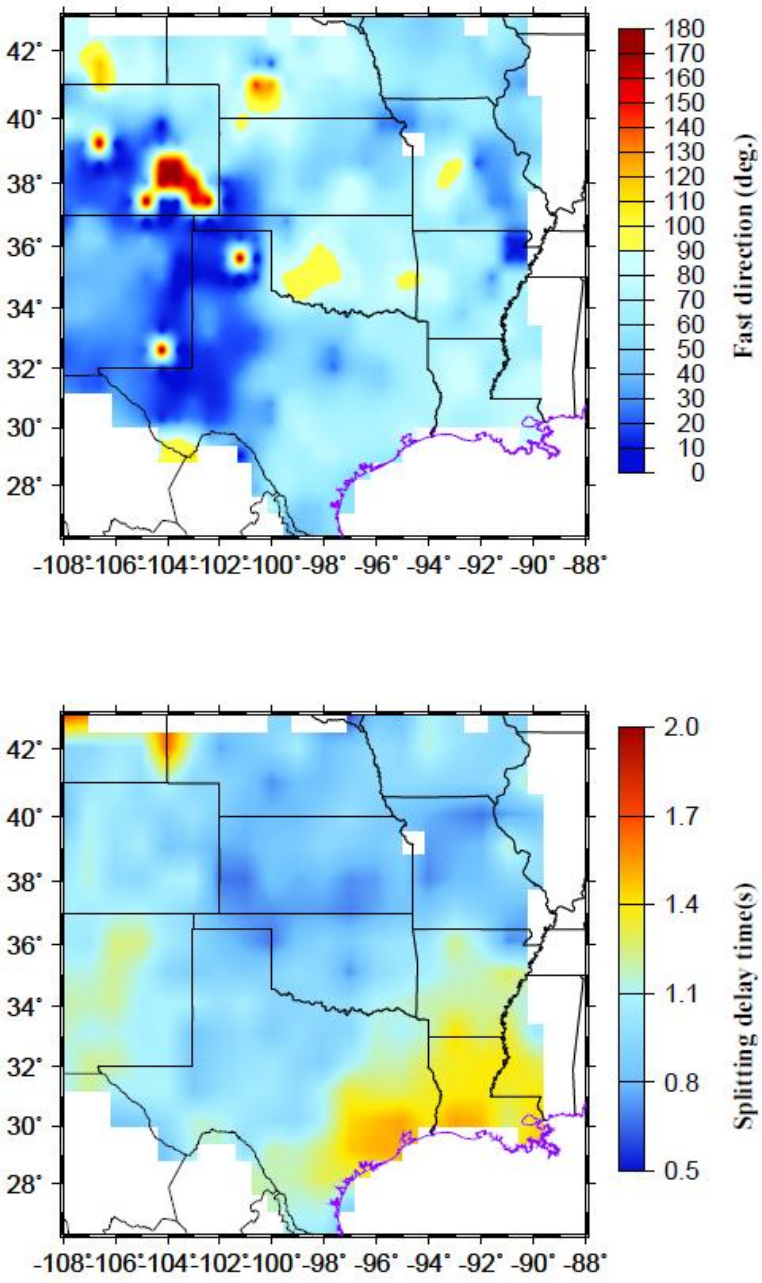

C12. Spatial distribution of Φ and δt. Our observation shows that the area with the largest splitting delay time is located near the transitional crust.

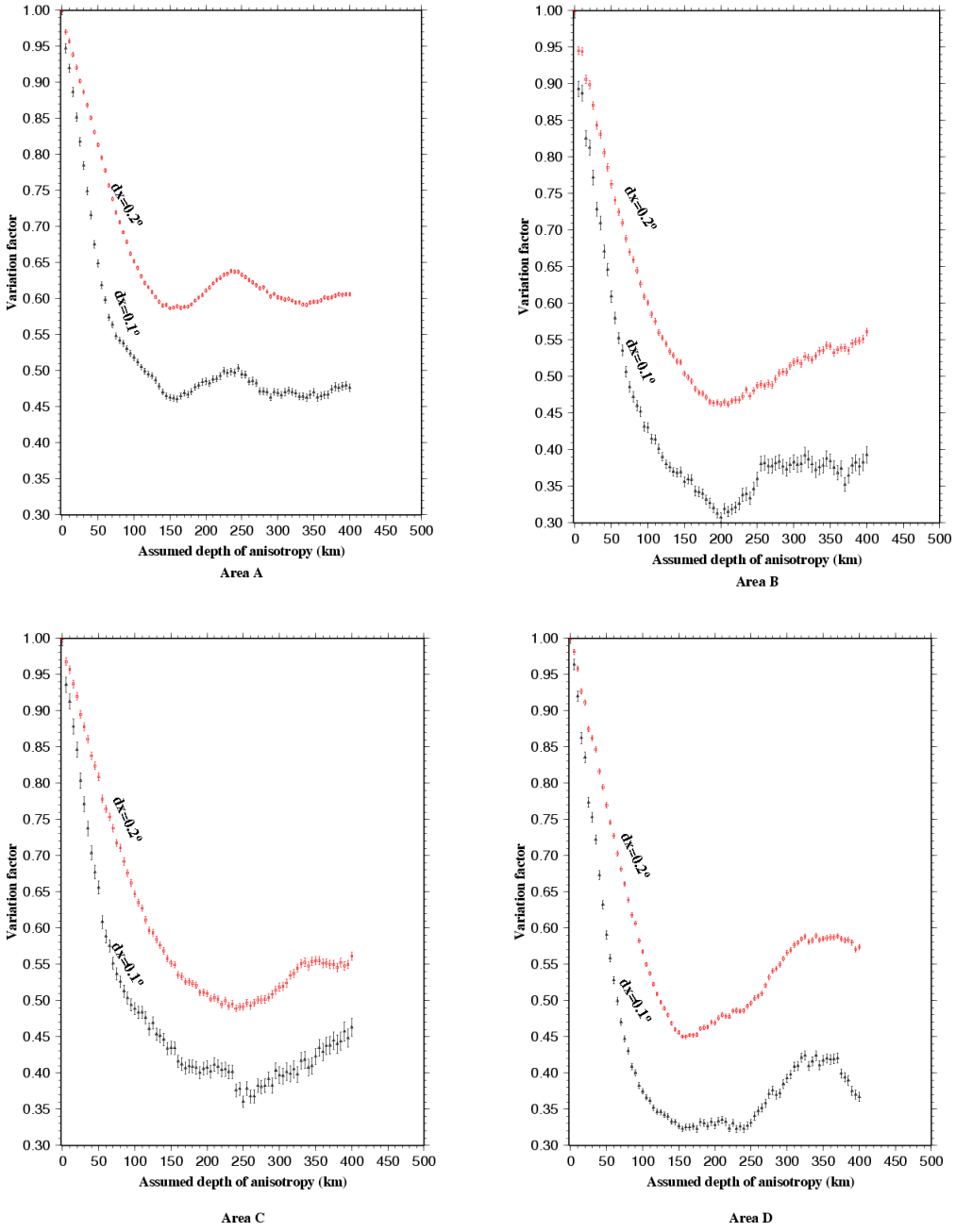

C14. Depth estimation for each of each of the four areas illustrated in Figure 1.3 in Section **1**

Table 1.Examples of some of shear wave splitting dataset for area **A** used in this study

Station	Phase	Lat	Lon	Φ	STD OF Φ	δt	STD of δt	BAZ	Rank
127Axx_TA	SKS	32.68	-103.36	5	20.5	0.45	0.22	247.84	B
127Axx_TA	SKS	32.68	-103.36	0	20.5	0.4	0.2	247.9	A
128Axx_TA	SKS	32.62	-102.49	11	3.5	0.65	0.08	240.86	A
128Axx_TA	SKS	32.62	-102.49	5	8	0.95	0.23	246	B
128Axx_TA	SKS	32.62	-102.49	168	3.5	1.15	0.22	245.39	A
129Axx_TA	SKS	32.63	-101.87	179	11	0.55	0.2	237.79	A
129Axx_TA	SKS	32.63	-101.87	27	3.5	0.6	0.05	241.18	A
129Axx_TA	SKS	32.63	-101.87	11	15.5	0.5	0.25	250.16	A
129Axx_TA	SKS	32.63	-101.87	41	5.5	0.8	0.28	321.69	A
129Axx_TA	SKS	32.63	-101.87	21	8.5	0.45	0.08	244.73	A
129Axx_TA	SKS	32.63	-101.87	30	15	0.45	0.15	245.72	A
227Axx_TA	SKS	32.01	-103.29	16	9.5	0.7	0.15	310.96	A
228Axx_TA	SKS	32.12	-102.59	40	7	0.85	0.22	240.79	A
229Axx_TA	SKS	31.97	-101.81	25	9.5	1.4	0.38	313.41	A
229Axx_TA	SKS	31.97	-101.81	18	15	1.1	0.52	311.77	A
229Axx_TA	SKS	31.97	-101.81	9	7	0.95	0.18	250.18	A
230Axx_TA	SKS	31.89	-101.11	23	16.5	1.05	0.5	313.81	A
230Axx_TA	SKS	31.89	-101.11	27	6	1.2	0.32	312.16	A
230Axx_TA	SKS	31.89	-101.11	46	2	1.75	0.22	241.53	A
230Axx_TA	SKS	31.89	-101.11	42	3.5	1.4	0.15	248.39	A
230Axx_TA	SKS	31.89	-101.11	33	4.5	0.8	0.15	322.09	A
527Axx_TA	SKS	30.15	-103.61	9	3.5	1	0.1	310.73	A
527Axx_TA	SKS	30.15	-103.61	178	4	1.2	0.17	287.64	B
527Axx_TA	SKS	30.15	-103.61	5	12	0.65	0.18	320.8	A
528Axx_TA	SKS	30.16	-102.79	14	13	0.9	0.25	321.22	B
529Axx_TA	SKS	30.12	-102.22	16	5.5	1.2	0.22	311.47	A
530Axx_TA	SKS	30.15	-101.34	30	10	0.7	0.1	252.14	A
530Axx_TA	SKS	30.15	-101.34	58	7	1	0.13	14.88	A
627Axx_TA	SKS	29.45	-103.39	101	11.5	0.5	0.12	236.86	A
628Axx_TA	SKS	29.49	-102.89	121	5.5	0.8	0.1	237.09	B

Station	Phase	Lat	Lon	Φ	STD OF Φ	δt	STD of δt	BAZ	Rank
V28Axx_TA	SKS	35.75	-102.22	5	14.5	1.15	0.38	245.58	A
W26Axx_TA	SKS	35.09	-103.77	36	6.5	1.1	0.22	236.16	B
W26Axx_TA	SKS	35.09	-103.77	12	14	0.75	0.2	320.62	B
W27Axx_TA	SKS	35.06	-103.06	179	4.5	1.3	0.22	248.03	A
W28Axx_TA	SKS	35.26	-102.21	48	11	0.65	0.23	241.16	A
W29Axx_TA	SKS	35.12	-101.65	161	5	1.3	0.33	238.14	A
W29Axx_TA	SKS	35.12	-101.65	174	11.5	0.65	0.22	241.45	A
W29Axx_TA	SKS	35.12	-101.65	11	10.5	0.75	0.2	248.05	A
W29Axx_TA	SKS	35.12	-101.65	173	9	0.95	0.28	245.01	A
W29Axx_TA	SKS	35.12	-101.65	8	17.5	0.6	0.32	245.89	A
X27Axx_TA	SKS	34.65	-103.1	14	12.5	0.55	0.12	248.01	A
X28Axx_TA	SKS	34.52	-102.2	27	13	0.7	0.23	241.11	B
X28Axx_TA	SKS	34.52	-102.2	29	9	1	0.3	316.79	A
X28Axx_TA	SKS	34.52	-102.2	9	5	1.05	0.15	247.75	B
X28Axx_TA	SKS	34.52	-102.2	8	6.5	1	0.25	298.96	A
Y26Axx_TA	SKS	33.92	-103.82	9	2.5	1.05	0.1	247.62	B
Y26Axx_TA	SKS	33.92	-103.82	17	4.5	1	0.13	243.12	A
Y26Axx_TA	SKS	33.92	-103.82	18	9.5	0.9	0.17	236.91	A
Y26Axx_TA	SKS	33.92	-103.82	6	9.5	1.05	0.18	236.03	A
Y26Axx_TA	SKS	33.92	-103.82	4	6.5	1.15	0.2	242.02	A
Y26Axx_TA	SKS	33.92	-103.82	12	4.5	0.8	0.08	240.22	A
127Axx_TA	PKS	32.68	-103.36	126	10.5	0.4	0.15	288.57	B
230Axx_TA	PKS	31.89	-101.11	46	5	0.7	0.1	340.26	B
327Axx_TA	PKS	31.37	-103.49	153	12.5	0.25	0.05	287.47	B
327Axx_TA	PKS	31.37	-103.49	17	12.5	0.55	0.12	319.54	B
429Axx_TA	PKS	30.62	-101.89	28	6.5	1.1	0.15	73.25	B
430Axx_TA	PKS	30.79	-101.24	33	12.5	0.9	0.23	73.57	B
430Axx_TA	PKS	30.79	-101.24	19	12	0.8	0.23	73.58	B
530Axx_TA	PKS	30.15	-101.34	38	2.5	1.4	0.18	291.95	B
LTXxxx_US	PKS	29.33	-103.67	85	14	0.9	0.3	316.93	B
Y28Axx_TA	SKK	33.91	-102.25	39	11	1.05	0.28	286.06	B
Y29Axx_TA	SKK	33.86	-101.67	42	8.5	0.85	0.15	276.26	B
Z26Axx_TA	SKK	33.27	-103.98	22	13	0.85	0.32	263.75	B
Z27Axx_TA	SKK	33.31	-103.21	37	9	1.1	0.38	318.58	B
Z30Axx_TA	SKK	33.29	-101.13	15	5.5	1.35	0.28	304.3	B

Table 2.Examples of shear wave splitting dataset for area **B** used in this study

Station	Phase	Lat	Lon	Φ	STD of Φ	δt	STD of δt	BAZ	Rank
N35Axx_TA	SKS	40.86	-95.64	82	8.5	0.75	0.15	313.36	B
N35Axx_TA	SKS	40.86	-95.64	75	10.5	0.7	0.15	313.15	A
N35Axx_TA	SKS	40.86	-95.64	77	12.5	0.85	0.25	313.39	B
N35Axx_TA	SKS	40.86	-95.64	89	1.5	1.05	0.07	18.8	A
N35Axx_TA	SKS	40.86	-95.64	74	10.5	1.35	0.47	317.68	B
N35Axx_TA	SKS	40.86	-95.64	75	7	1.05	0.17	307.62	B
N35Axx_TA	SKS	40.86	-95.64	81	21	0.5	0.3	323.12	A
N35Axx_TA	SKS	40.86	-95.64	86	6	1.15	0.27	282.81	A
N36Axx_TA	SKS	40.82	-94.96	67	12.5	0.75	0.3	314.23	A
N36Axx_TA	SKS	40.82	-94.96	75	3.5	1.35	0.15	19.4	A
N36Axx_TA	SKS	40.82	-94.96	73	18	0.65	0.25	320.03	A
N36Axx_TA	SKS	40.82	-94.96	78	11	0.85	0.2	308.25	B
N36Axx_TA	SKS	40.82	-94.96	61	8.5	0.95	0.18	281.54	B
N36Axx_TA	SKS	40.82	-94.96	59	12.5	0.8	0.23	267.34	B
N36Axx_TA	SKS	40.82	-94.96	71	2.5	1.25	0.13	10.53	B
N36Axx_TA	SKS	40.82	-94.96	82	8.5	1.45	0.35	316.51	B
N36Axx_TA	SKS	40.82	-94.96	77	13	0.8	0.17	31.27	A
N36Axx_TA	SKS	40.82	-94.96	68	3	0.9	0.17	323.65	A
N36Axx_TA	SKS	40.82	-94.96	67	11	0.9	0.2	283.29	A
O35Axx_TA	SKS	40.27	-95.91	16	10.5	0.75	0.2	313.37	A
O35Axx_TA	SKS	40.27	-95.91	11	8	0.85	0.17	318.23	B
O35Axx_TA	SKS	40.27	-95.91	25	13.5	0.6	0.22	322.84	A
O36Axx_TA	SKS	40.13	-94.96	28	12.5	1.65	0.7	310.14	A
O36Axx_TA	SKS	40.13	-94.96	35	2.5	0.95	0.12	19.48	A
O36Axx_TA	SKS	40.13	-94.96	33	16	0.6	0.2	10.55	B
O36Axx_TA	SKS	40.13	-94.96	27	14.5	0.65	0.2	341.52	B
O36Axx_TA	SKS	40.13	-94.96	15	8	0.4	0.05	323.56	A
P36Axx_TA	SKS	39.62	-95.21	33	2	0.95	0.15	19.32	A
P36Axx_TA	SKS	39.62	-95.21	26	9	0.6	0.15	323.29	B
Q36Axx_TA	SKS	38.96	-95.46	50	9	0.9	0.25	297.89	B
Q36Axx_TA	SKS	38.96	-95.46	78	6.5	1.15	1.38	248.2	A
N32Axx_TA	SKK	40.76	-98.3	71	4	0.9	0.1	310.6	A
N32Axx_TA	SKS	40.76	-98.3	90	3.5	0.75	0.08	310.85	B

Station	Phase	Lat	Lon	Φ	STD OF Φ	δt	STD of δt	BAZ	Rank
N32Axx_TA	SKS	40.76	-98.3	77	2	1.6	0.28	265.2	A
N33Axx_TA	PKS	40.74	-97.45	64	5.5	0.95	0.17	308.51	B
N33Axx_TA	SKK	40.74	-97.45	63	3.5	1.05	0.13	311.59	B
N33Axx_TA	SKK	40.74	-97.45	65	2	1.05	0.1	311.38	A
N33Axx_TA	SKK	40.74	-97.45	58	11	1	0.23	293.68	B
N33Axx_TA	SKS	40.74	-97.45	54	6.5	0.9	0.2	298.86	B
N33Axx_TA	SKS	40.74	-97.45	65	6.5	0.95	0.17	280.01	B
N33Axx_TA	SKS	40.74	-97.45	55	4.5	1.1	0.28	311.38	A
N33Axx_TA	SKS	40.74	-97.45	56	2.5	1.15	0.08	283.1	B
N33Axx_TA	SKS	40.74	-97.45	44	6	0.75	0.12	262.24	B
N33Axx_TA	SKS	40.74	-97.45	75	12	0.5	0.1	312.51	A
N33Axx_TA	SKS	40.74	-97.45	60	5	0.9	0.12	9.73	B
N33Axx_TA	SKS	40.74	-97.45	54	4	0.75	0.08	265.73	B
N33Axx_TA	SKS	40.74	-97.45	64	4.5	1.05	0.13	8.63	B
N33Axx_TA	SKS	40.74	-97.45	51	10.5	0.7	0.2	268.91	B
N34Axx_TA	PKS	40.84	-96.5	58	4	0.9	0.15	348.91	A
N34Axx_TA	PKS	40.84	-96.5	66	3	1.15	0.13	309.66	A
N34Axx_TA	SKK	40.84	-96.5	69	5	1.05	0.15	312.32	A
N34Axx_TA	SKK	40.84	-96.5	86	3	1.65	0.23	18.03	A
N34Axx_TA	SKK	40.84	-96.5	55	12.5	0.8	0.3	257.65	A
N34Axx_TA	SKS	40.84	-96.5	77	16.5	0.65	0.25	312.32	A
N34Axx_TA	SKS	40.84	-96.5	-83	9	0.65	0.12	313.17	B
N34Axx_TA	SKS	40.84	-96.5	88	13	0.65	0.15	311.8	B
N34Axx_TA	SKS	40.84	-96.5	81	1.5	1.45	0.08	18.03	A
N34Axx_TA	SKS	40.84	-96.5	66	5.5	1	0.15	10.5	B
N34Axx_TA	SKS	40.84	-96.5	46	12.5	0.65	0.15	266.36	B
N34Axx_TA	SKS	40.84	-96.5	76	4	1.2	0.17	9.36	B
O29Axx_TA	PKS	40.13	-100.8	61	2.5	1.35	0.2	343.23	A
O29Axx_TA	PKS	40.13	-100.8	-85	9.5	0.5	0.1	304.43	A
P34Axx_TA	SKS	39.55	-96.83	62	3.5	1.05	0.12	305.85	B
P34Axx_TA	SKS	39.55	-96.83	62	8	0.95	0.2	297.05	B
L36Axx_TA	SKS	42.1	-94.67	43	5.5	1	0.2	19.52	A
L36Axx_TA	SKS	42.1	-94.67	36	7	1	0.23	10.72	A

Table 3.Examples of shear wave splitting dataset for area **C** used in this study

Station	Phase	Lat	Lon	Φ	STD of Φ	δt	STD of δt	BAZ	Rank
MM18xx_XA	SKS	38.53	-90.57	69	7	1.15	0.25	283.29	B
MM18xx_XA	SKS	38.53	-90.57	68	4.5	1.2	0.3	260.36	A
MM18xx_XA	SKS	38.53	-90.57	57	5	0.95	0.1	284.26	A
N38Axx_TA	SKS	40.79	-93.24	75	6.5	0.8	0.12	20.92	A
S38Axx_TA	SKS	37.63	-93.91	46	16.5	0.65	0.32	282.46	A
S39Axx_TA	SKS	37.69	-93.32	89	6.5	0.5	0.12	21.23	A
S39Axx_TA	SKS	37.69	-93.32	94	10.5	0.7	0.18	308.15	A
S39Axx_TA	SKS	37.69	-93.32	76	6	0.7	0.13	282.91	A
S40Axx_TA	SKS	37.6	-92.5	45	5	0.8	0.12	21.97	A
S40Axx_TA	SKS	37.6	-92.5	77	11	0.95	0.3	281.91	A
S40Axx_TA	SKS	37.6	-92.5	77	8	0.7	0.18	12.52	B
S40Axx_TA	SKS	37.6	-92.5	52	9	0.8	0.17	283.44	A
S42Axx_TA	SKS	37.77	-90.79	36	9	1.15	0.28	284.76	A
S42Axx_TA	SKS	37.77	-90.79	44	10.5	0.85	0.25	254.39	B
T39Axx_TA	SKS	37.02	-93.38	66	8	0.8	0.15	281.06	A
T39Axx_TA	SKS	37.02	-93.38	71	12	0.7	0.18	282.52	A
T40Axx_TA	SKS	37.15	-92.52	52	5.5	0.9	0.13	22.02	A
T40Axx_TA	SKS	37.15	-92.52	59	9.5	0.75	0.12	12.53	A
T41Axx_TA	SKS	37.04	-91.76	56	15.5	0.85	0.28	283.66	A
T42Axx_TA	SKS	37.03	-91.09	33	5	1.05	0.2	284.13	A
N38Axx_TA	PKS	40.79	-93.24	62	6.5	0.95	0.23	313.44	A
N38Axx_TA	PKS	40.79	-93.24	72	4.5	0.8	0.08	302.82	A
N39Axx_TA	PKS	40.88	-92.5	56	3	1	0.1	303.63	A
N40Axx_TA	PKS	40.88	-91.58	47	2	1.65	0.22	304.58	A
O39Axx_TA	PKS	40.25	-92.54	76	7	0.45	0.1	313.87	A
P38Axx_TA	PKS	39.62	-93.53	40	13	0.5	0.15	329.9	B
P38Axx_TA	PKS	39.62	-93.53	49	4.5	0.8	0.15	301.68	A
Q38Axx_TA	PKS	38.96	-93.62	88	14	0.45	0.1	311.52	A
Q38Axx_TA	PKS	38.96	-93.62	71	10.5	0.65	0.17	299.63	B
Q38Axx_TA	PKS	38.96	-93.62	62	11.5	0.6	0.2	301.1	A
Q38Axx_TA	PKS	38.96	-93.62	63	3.5	1.3	0.35	343.02	A

Station	Phase	Lat	Lon	Φ	STD OF Φ	δt	STD of δt	BAZ	Rank
R38Axx_TA	PKS	38.19	-93.91	85	6.5	0.65	0.1	310.52	A
R38Axx_TA	PKS	38.19	-93.91	61	11.5	0.55	0.17	300.24	A
R39Axx_TA	PKS	38.31	-93.04	96	8.5	0.75	0.15	311.67	A
R39Axx_TA	PKS	38.31	-93.04	93	3	0.8	0.1	301.18	A
R41Axx_TA	PKS	38.3	-91.38	162	13.5	0.35	0.12	312.05	A
R42Axx_TA	PKS	38.28	-90.79	63	5.5	0.95	0.17	312.67	B
S38Axx_TA	PKS	37.63	-93.91	77	5.5	0.5	0.05	310.04	A
S38Axx_TA	PKS	37.63	-93.91	65	10	0.65	0.1	299.81	A
S39Axx_TA	PKS	37.69	-93.32	89	6.5	0.65	0.08	310.8	A
S39Axx_TA	PKS	37.69	-93.32	95	8	0.75	0.17	298.94	B
S39Axx_TA	PKS	37.69	-93.32	79	5.5	0.7	0.15	328.87	B
S39Axx_TA	PKS	37.69	-93.32	86	6.5	0.8	0.1	300.43	A
S39Axx_TA	PKS	37.69	-93.32	107	5.5	0.7	0.15	309.63	B
S40Axx_TA	PKS	37.6	-92.5	86	6.5	0.7	0.1	311.72	B
S41Axx_TA	PKS	37.59	-91.75	75	9.5	0.4	0.08	304.22	B
S42Axx_TA	PKS	37.77	-90.79	49	5.5	0.85	0.2	303.01	A
T40Axx_TA	PKS	37.15	-92.52	52	8	0.9	0.25	300.78	B
T40Axx_TA	PKS	37.15	-92.52	64	5.5	0.75	0.15	310.11	B
T41Axx_TA	PKS	37.04	-91.76	79	12	0.55	0.12	301.45	A
V37Axx_TA	SKS	35.88	-95.14	66	10	0.9	0.18	10.57	A
W30Axx_TA	SKS	35.18	-100.58	148	5.5	0.9	0.17	259.28	A
W31Axx_TA	SKS	35.19	-99.94	77	2.5	0.95	0.07	15.54	A
W36Axx_TA	SKS	35.14	-96.23	89	6.5	0.8	0.17	250	B
W36Axx_TA	SKS	35.14	-96.23	63	2	0.85	0.05	18.97	A
W36Axx_TA	SKS	35.14	-96.23	80	5	1.05	0.17	9.76	B
S35Axx_TA	SKS	37.68	-96.32	-50	17.5	0.55	0.25	249.09	A
U33Axx_TA	SKS	36.43	-98.11	81	11.5	1	0.32	8.24	B
U34Axx_TA	PKS	36.44	-97.54	89	15.5	0.55	0.2	304.87	A
U34Axx_TA	SKS	36.44	-97.54	56	20	0.55	0.3	17.6	A
U34Axx_TA	SKS	36.44	-97.54	79	3.5	0.9	0.15	8.69	B
U35Axx_TA	SKK	36.37	-96.73	48	10	1.05	0.45	337.46	A
U35Axx_TA	SKS	36.37	-96.73	68	7	0.65	0.1	18.35	A
U35Axx_TA	SKS	36.37	-96.73	65	7	0.75	0.1	9.32	A

Table 4.Examples of shear wave splitting dataset for area **D** used in this study

Station	Phase	Lat	Lon	Φ	STD OF Φ	δt	STD OF δt	BAZ	Rank
V38Axx_TA	SKS	35.86	-94.41	91	8	0.95	0.15	311.96	A
V38Axx_TA	SKS	35.86	-94.41	76	14	1.05	0.4	301.2	B
V38Axx_TA	SKS	35.86	-94.41	47	12	0.75	0.15	11.14	A
V38Axx_TA	SKS	35.86	-94.41	51	15	1.1	0.4	31.87	A
V39Axx_TA	SKS	35.84	-93.64	51	4	0.9	0.08	280.37	B
V39Axx_TA	SKS	35.84	-93.64	65	17.5	0.7	0.35	266.82	A
V39Axx_TA	SKS	35.84	-93.64	68	10.5	0.95	0.2	11.73	B
V40Axx_TA	SKS	35.8	-92.82	67	6	1	0.12	12.36	B
131Axx_TA	SKS	32.67	-100.39	23	4.5	0.65	0.13	310.05	A
131Axx_TA	SKS	32.67	-100.39	50	5	0.9	0.12	15.44	A
131Axx_TA	SKS	32.67	-100.39	17	10	0.7	0.13	243.81	B
133Axx_TA	SKS	32.61	-98.92	50	7	0.95	0.23	249.55	A
133Axx_TA	SKS	32.61	-98.92	58	2.5	1.4	0.2	342.7	A
133Axx_TA	SKS	32.61	-98.92	42	3.5	0.75	0.1	247.92	B
133Axx_TA	SKS	32.61	-98.92	47	4.5	0.95	0.2	246.22	A
133Axx_TA	SKS	32.61	-98.92	60	5	1.3	0.3	306.09	A
133Axx_TA	SKS	32.61	-98.92	74	11.5	0.9	0.2	306.32	B
133Axx_TA	SKS	32.61	-98.92	69	2.5	1.35	0.3	259.7	A
133Axx_TA	SKS	32.61	-98.92	45	2.5	0.8	0.08	247.27	A
133Axx_TA	SKS	32.61	-98.92	52	2	1.05	0.18	310.94	A
133Axx_TA	SKS	32.61	-98.92	59	18	0.9	0.38	309.49	A
133Axx_TA	SKS	32.61	-98.92	57	3.5	1.4	0.25	253.75	A
133Axx_TA	SKS	32.61	-98.92	65	10.5	0.9	0.2	304.45	B
133Axx_TA	SKS	32.61	-98.92	49	3	1.05	0.2	244.19	A
133Axx_TA	SKS	32.61	-98.92	51	9	0.75	0.2	249.76	A
133Axx_TA	SKS	32.61	-98.92	56	3.5	1.15	0.17	254.21	A
133Axx_TA	SKS	32.61	-98.92	67	6.5	0.95	0.28	263.21	A
133Axx_TA	SKS	32.61	-98.92	56	5	0.9	0.13	290.05	B
133Axx_TA	SKS	32.61	-98.92	67	4	1.35	0.15	7.75	A
133Axx_TA	SKS	32.61	-98.92	52	4	1.15	0.25	247.54	B
133Axx_TA	SKS	32.61	-98.92	45	3.5	1	0.18	245.51	A
133Axx_TA	SKS	32.61	-98.92	50	3	1.15	0.2	245.71	B
134Axx_TA	SKS	32.57	-98.08	34	10	0.7	0.12	249.99	A

Station	Phase	Lat	Lon	Φ	STD OF Φ	δt	STD OF δt	BAZ	Rank
134Axx_TA	SKS	32.57	-98.08	65	6.5	1.2	0.32	260.12	A
134Axx_TA	SKS	32.57	-98.08	29	8	0.65	0.1	247.7	A
531Axx_TA	PKS	30.16	-100.55	43	5.5	1.1	0.23	292.63	B
533Axx_TA	PKS	30.07	-99.04	64	12	0.65	0.15	297.24	A
534Axx_TA	PKS	30.03	-98.48	81	4.5	0.6	0.08	287.35	A
534Axx_TA	PKS	30.03	-98.48	74	7	0.95	0.15	297.74	A
535Axx_TA	PKS	30.03	-97.57	60	11.5	0.6	0.17	288.01	B
535Axx_TA	PKS	30.03	-97.57	65	4.5	1.25	0.15	298.63	B
536Axx_TA	PKS	30.08	-97.07	73	8	1.5	0.35	287.22	B
537Axx_TA	PKS	30.08	-96.32	71	4	1.35	0.15	288.98	B
633Axx_TA	PKS	29.46	-99.18	70	9	0.85	0.18	296.47	B
634Axx_TA	PKS	29.38	-98.35	80	2	1.1	0.1	286.91	B
634Axx_TA	PKS	29.38	-98.35	60	9	1.05	0.27	289.28	B
635Axx_TA	PKS	29.39	-97.77	67	5	1.35	0.17	287.33	B
635Axx_TA	PKS	29.39	-97.77	64	3.5	1.4	0.12	289.4	B
733Axx_TA	PKS	28.72	-99.29	61	8.5	1.15	0.28	295.59	A
733Axx_TA	PKS	28.72	-99.29	39	9	0.9	0.28	288.04	B
933Axx_TA	SKK	27.61	-99.27	59	3	1.4	0.12	275	B
934Axx_TA	SKK	27.6	-98.52	47	4	1.35	0.15	275.37	B
ABTXxx_TA	SKK	32.62	-99.64	42	3.5	1.2	0.13	276.95	B
ABTXxx_TA	SKK	32.62	-99.64	44	14	0.65	0.25	245.86	B
X37Axx_TA	SKK	34.59	-95.37	78	13	0.9	0.25	310.38	B
X41Axx_TA	SKK	34.49	-92.51	42	14	0.9	0.25	343.17	B
Y30Axx_TA	SKK	33.88	-100.9	39	8.5	1.4	0.3	276.73	B
Y30Axx_TA	SKK	33.88	-100.9	28	4.5	1.5	0.3	14.79	B
Y31Axx_TA	SKK	33.96	-100.26	41	3	1.5	0.12	277.14	B
Y32Axx_TA	SKK	34	-99.44	59	4	1.2	0.12	277.65	B
Y32Axx_TA	SKK	34	-99.44	57	6.5	0.65	0.13	306.38	A
Y32Axx_TA	SKK	34	-99.44	70	18.5	0.55	0.25	306.79	B
Y33Axx_TA	SKK	34.01	-98.63	176	5	0.95	0.2	245.79	B
Y37Axx_TA	SKK	33.98	-95.62	78	8.5	1.15	0.3	238.2	B
Y39Axx_TA	SKK	33.94	-94.09	61	7.5	1.5	0.48	311.24	B
Z31Axx_TA	SKK	33.32	-100.14	32	3	1.6	0.17	276.95	B

REFERENCES

Balch, R.S., Hartse, H.E., Sanford, A.R., Lin, K.W., 1997. A new map of the geographic extent of the Socorro mid-crustal magma body, Bull. Seismo. Soc. Amer., 87, 174-182.

Baldridge, W.S., Perry, F.V., Vaniman, D.T., Nealey, L.D., Leavy, B.D., Laughlin, A.W., Kyle, P.R., Bartov, Y., Steintz, G., Gladney, E.S., 1991. Middle to late Cenozoic magmatism of the southeastern Colorado Plateau and central Rio Grande rift (New Mexico and Arizona, USA): A model for continental rifting, Tectonophysics, 197, 327-354.

Barruol, G., Silver, P.G., Vauchez, A., 1997. Seismic anisotropy in the eastern United States: Deep structure of complex continental plate, J. Geophys. Res., 102, 8329-8348, DOI:10.1029/96JB03800.

Barruol, G., Hoffmann, R., 1999. Upper Mantle anisotropy beneath the Geoscope stations, J. Geophys. Res., 104, 10757-10773.

Becker, T.W., O'Connell, R., 2001. Predicting plate velocities with mantle circulation models, Geochem. Geophys. Geosyst., 2, DOI:10.1029/2001GC000171.

Bird, P., Liu, Z., Rucker, W.K., 2008. Stress that drive the plates from below: Definitions, computational path, model optimization, and error analysis, J. Geophys. Res., 113, B11406, DOI:10.1029/2007JB005460.

Burdick , S., Van Der Hilst, R.D., Vernon, F.L., Martynov, V., Cox, T., Eakins, J., Karasu, G.H., Tylell, J., Astiz, L., Pavlis, G.L., 2012. Model update March 2011: Upper mantle heterogeneity 559 beneath North America from traveltime tomography with global and USArray Transportable Array data, Seismo. Res. Lett., 83, 23-28, DOI:10.1785/gssrl.83.1.23.

.Condie, K.C., 1982. Plate-tectonics model for Proterozoic continental accretion in the southwestern United States, Geology, 10, 37-42. Coward, M.P., Butler, R.W.H., Khan, M.A., Knipe, R.J., 1987. The tectonic history of Kohistan and its implications for Himalayan structure, J. Geol. Soc., London, 144, 377-391.

Conrad, C.P., Behan, M.D., Silver, P.G., 2007. Global mantle flow and the development of seismic anisotropy: differences between the oceanic and the continental upper mantle, J. Geophys. Res., 112, B07317. DOI:101029/2006JB004608.

Coward, M.P., Butler, R.W.H., Khan, M.A., Knipe, R.J., 1987. The tectonic history of Kohistan and its implications for Himalayan structure, J. Geol. Soc., London, 144, 377-391.

Craig, C.H., McKenzie, D., 1986. The existence of a thin low-viscosity layer beneath the lithosphere, Earth Planet. Sci. Lett., 78, 420-426.

Debayle, E., Kennett, B.L.N., Priestley, K., 2005. Global azimuthal seismic anisotropy and the unique plate-motion deformation of Australia, Science, 433, 509-512.

Doglioni, C., Ismail-Zadeh, A., Panza, G., Riguzzi F., 2011. Lithosphere-asthenosphere viscosity contrast and decoupling, Phys. Earth Planet. Inter., 189, 1-8.

Fouch, M.J., Fischer, K.M., Parmentier, E.M., Wysession, M.E., Clarke, T.J., 2000. Shear wave splitting, continental keels, and pattern of mantle flow, J. Geophys. Res., 105, 6255-6275.

Fouch, M.J., Rondenay, S., 2006. Seismic anisotropy beneath stable continental interiors,Phys.EarthPlanet.Inter,158,292-320, DOI:10.1016/j.pepi.2006.01.022.

Gao, S.S., Davis, P.M., Liu, K.H., Slack, P.D., Rigor, A.W., Zorin, Y.A., Mordvinova, V.V., Kozhevnikov, V.M., Logatchev, N.A., 1997. SKS splitting beneath continental rift zones, J. Geophys. Res., 102, 22781-22797.

Gao, S.S., Liu, K.H., 2009. Significant seismic anisotropy beneath the southern Lhasa Terrane, Tibetan Plateau, Geochem. Geophys. Geosyst., 10, 597 Q02008, DOI:10.1029/2008GC002227.

Gao, S.S., Liu, K.H., 2012. AnisDep: A FORTRAN program for the estimation of the depth of anisotropy using spatial coherency of shear-wave splitting parameters, Compu. Geosci., DOI: 10.1016/j.cageo.2012.01.020.

Gao, S.S., Liu, K.H., Abdelsalam, M.G., 2010. Seismic anisotropy beneath the Afar Depression and adjacent areas: Implications for mantle flow, J. Geophys. Res., 115, B12330, DOI: 10.1029/2009JB007141.

Gao, S.S., Liu, K.H., Stern, R.J., Keller, G.R., Hogan, J.P., Pulliam, J., Anthony, E.Y., 2008. Characteristics of mantle fabrics beneath the southcentral United States: Constraints from shear-wave splitting measurements, Geosphere, 4, 411-417, DOI:10.1130/GES00159.1.

Gok, R., Ni, J., Sandvol, E., Wilson, D., Baldridge, W.S., Aster, R., West, M., Grand, S., Gao, W., Tilmann, F., Semken, S., 2003. Shear wave splitting and mantle flow beneath the LA RISTRA array, J. Geophys. Res., 115, B12330, DOI: 10.1029/2009JB007141.

Gripp, A.E., Gordon, R.G., 2002. Young tracks of hotspots and current plate velocities, Geophys. J. Int., 150, 321-361.

Hoffman, P.F., 1988. United plates of America, the birth of a craton: early Proterozoic assembly and growth in Laurentia, Annu. Rev. Earth Planet. Sci., 16, 543-603.

Hoffman, P.F., 1989. Precambrian geology and tectonic history of North America, in Bally, A.W., and Palmer, A. R., eds., The geology of North America- An overview, Geol. Soc. Amer., 447-512.

Huang, Z., Wang, L., Zhao, D., Mi, N., Xu, M., 2011. Seismic anisotropy and mantle dynamics beneath China, Earth Planet. Sci. Lett., 306, 105-117.

James, D.E., Fouch, M.J., VanDecar, J.C., van der Lee, S., Kaapvaal Seismic Group, 2001. Tectospheric structure beneath southern Africa, Geophys. Res. Lett., 28, 2485-2488.

Karato, S., Jung, H., Katayama, I., Skemer, P., 2008. Geodynamic significance of the seismic anisotropy of the upper mantle: New insights from laboratory studies, Annu. Rev. Earth Planet. Sci., 36, 59-95.

Karlstrom, K.E., Bowring, S.A., 1988. Early Proterozoic assembly of tectono-stratigraphic terranes in southwestern North America, J. Geology, 96, 561-576.

Karlstrom, K.E., Humphreys, E.D., 1998. Persistent influence of Proterozoic accretionary boundaries in the tectonic evolution of southwestern North America: Interaction of cratonic grain and mantle modification events, Rocky Mountain Geology, 33, 161-179.

.Kendall, J.-M., Stuart, G.W., Ebinger, C., Bastow, I.D., Keir, D., 2005, Magma-assisted rifting in Ethiopia, Nature, 433, 146-148.

Lawton, T.F., McMillan, N.J., 1999. Arc abandonment as a cause for passive continental rifting: Comparison of the Jurassic Mexican Borderland rift and the Cenozoic Rio Grande rift, Geology, 27, 779-782.

Liu, K.H., 2009. NA-SWS- 1.1: A uniform database of teleseismic shear-wave splitting measurements for North America, Geochem. Geophys. Geosyst., 10, Q05011, DOI:10.1029/ 2009 GC002440.

Liu, K.H., Gao, S.S., 2010. Spatial variations of crustal characteristics beneath the Hoggar swell, Algeria revealed by systematic analyses of receiver functions from a single seismic station, Geochem. Geophys. Geosys., 11, Q08011, DOI:10.1029/2010GC003091.

Liu, K.H., Gao, S.S., 2011. Estimation of the depth of anisotropy using spatial coherency of shear-wave splitting parameters, Bull. Seismo. Soc. Amer., 101, 2153-2161.

Liu, L., Gurnis, M., 2010. Dynamic subsidence and uplift of the Colorado Plateau, Geology, 38, 719-722.

Liu, K.H., Gao, S.S., Gao, Y., Wu J., 2008. Shear wave splitting and mantle flow associated with the deflected slab beneath northeast Asia, J. Geophys. Res., 113, B01305, DOI:10.1029/2007JB005178.

Long, M.D., Silver, P.G., 2009. Shear wave splitting anisotropy: Measurements, Interpretation, and new Directions, Survey Geophys., 407-461.

Mainprice, D., Barruol, G., Ben Ismail, W., 2000. The seismic anisotropy of the Earth's Mantle: From single crystal to polycrystal, in Earth's Deep Interior: Mineral Physics and Tomography From the Atomic to the Global Scale, edited by S. I. Karato, 237-264, AGU, Washington, D.C.

Marone, F., Romanowicz, B., 2007. The depth distribution of azimuthal anisotropy in the continental upper mantle, Nature, 447, 198-201.

McMillan, J., Dickin, A.P., Haag, D., 2000. Evolution of magma source regions in the Rio Grande rift, southern New Mexico, Geol. Soc. Amer. Bull., 112, 1582-1593.

Mickus, K., Stern, R.J., Keller, G.R., Anthony, E.Y., 2009. Potential field evidence for a volcanic rifted margin along the Texas Gulf Coast, Geology, 37, 387-390, DOI: 10.1130/G25465A.1.

Montagner, J., 1998.Where can seismic anisotropy be detected in the Earth's mantle? in boundary layers ..., Pure Appl. Geophys., 151, 223-256.

Morgan, P., Seager, W.R., Golombek, M.P., 1986. Cenozoic thermal mechanical and tectonic evolution of the Rio Grande rift, J. Geophys. Res., 91, 6262-6276.

Mosher, S., 1998. Tectonic evolution of the southern Laurentian Grenville orogenies belt, Geol. Soc. Amer. Bull., 110, 1357-1375.

Nicolas, A., 1993. Why fast polarization directions of SKS seismic waves are parallel to mountainbelts, Phys. Earth Planet. Int., 78, 337-342.

Nicolas, A., Christensen, N.I., 1987. Formation of anisotropy in upper mantle peridotites: A review, in composition structure and Dynamics of the Lithosphere-Asthenosphere System, Geodyn. Ser., 16, edited by K. Fuchs and C. Froidevaux, 338-343.

Sandvol, E., Ni, J., Ozalaybey, S., Schlue, J., 1992, Shear-wave splitting in the Rio Grande Rift, Geophys. Res. 670 Lett., 19, 2337-2340, DOI:10.1029/92GL02715.

Savage, M.K., 1999. Seismic anisotropy and mantle deformation: what we learned from shear - wave splitting?, Rev. Geophys., 37, 65-106.

Savage, M.K., Sheehan, A.F., 2000. Seismic anisotropy and mantle flow from the Great Basin to the Great Plains, western United States, J. Geophys. Res., 151,443-462.

Silver, P.G., 1996. Seismic anisotropy beneath the continents: Probing the depths of geology, Annu. Rev. Earth Planet. Sci., 24, 385-432.

Silver, P.G., Chan, W.W., 1988. Implications for continental structure and evolution from seismic anisotropy, Nature, 335, 34-39.

Silver, P.G., Chan, W.W., 1991. Shear wave splitting and subcontinental mantle deformation, J. Geophys. Res., 96, 16,429-16,454.

Silver, P.G., Savage, M., 1994. The interpretation of shear-wave splitting parameters in the presence of two anisotropic layers, Geophys. J. Int., 119, 949-963, DOI:10.1111/j.1365-246X.1994.tb04027.x.

Thomas, W.A., 2006. Tectonic inheritance at a continental margin, GSA Today, 16, 4-11.

Tommasi, A., Mainprice, D., Cordier, P., Thoraval, C., Couvy, H., 2004. Strain-induced seismic anisotropy of wadsleyite polycrystals and flow patterns in the mantle transition zone, J. Geophys. Res., 109, B12405, DOI:10.1029/2004JB003158.

VanDecar, J.C., Crossen, R.S., 1990. Determination of teleseismic relative phases arrival times using multi-channel cross-correlation and least-squares, Bull. Seismo. Soc. Amer., 80, 150-169.

van der Lee, S., Frederiksen, A., 2005. Surface wave tomography applied to the North American upper mantle, in Nolet, G., and Levander, A., eds., Seismic data analysis and imaging with global and local arrays, Amer. Geophys. Union Monograph, 157, 67-80.

van der Lee, S., Nolet, G., 1997. Upper mantle S velocity structure of North America, J. Geophys.Res., 102, 22815-22838, I:10.1029/97JB01168.

Wang, X., Ni, J.F., Aster, R., Sandvol, E., Wilson, D., Sine, C., Grand, S.P., Baldridge, W.S, 2008. Shear-wave splitting and mantle flow beneath the Colorado Plateau and its boundary with the Great Basin. Bull. Seismo. Soc. Amer., 98, 2526-2532.

Wessel, P., Smith, W.H.F., 1991. Free software helps map and display data, Eos, Trans. AGU 72, 441, 445-446.

Whitmeyer, S.J., Karlstrom, K.E., 2007. Tectonic model 713 for the Proterozoic growth of North America, Geosphere, 34, 220-259.

Wilson, D., Aster, R., West, W., Ni, J., Grand, S., Gao,W., Baldridge, W.S., Patel, P., 2005. Lithospheric structure of the Rio Grande rift, Nature, 433, 851-855.

Yuan, H., Romanowicz, B., 2010, Lithospheric layering in the North American craton, Nature, 466, 1063-1069.

Zhang, S., Karato, S.I., 1995. Lattice preferred orientation of olivine aggregates deformed in simple shear, Nature, 375, 774-777.

VITA

Hesham Refayee was born in a coastal ancient Roman city called El-Khoms. In 1998, he received his Bachelor's degree in Geology from Tripoli University (Formly El-Fateh University), Tripoli, Libya and a Master degree in Geology and Geophysics from Missouri University of Science and Technology, Rolla in 2008. In January 2009, he joined the PhD program in Geology and Geophysics at Missouri University of Science and Technology.

Hesham was involved in many graduate student activities, he taught several geophysical courses during his stay at Missouri &ST. He was an active member in the Society of Exploration Geophysics (SEG), American Geophysical Union (AGU), American Association of Petroleum Geologist (AAPG), Society of Petroleum Engineering (SPE), and Geologic Society of America (GSA).

During his graduate studies, he participated in several annual meetings. In 2008, he presented his research at the annual meeting of the GSA in Houston, TX. In 2010, he presented part of his research at the regional meeting of the GSA in Branson, MO. In 2011, his poster was chosen as the best student poster in the ESSSA in Little Rock, AR. He also presented in the annual meeting of the AGU in 2011 held in San Francisco, CA.

Hesham was awarded the Spooner outstanding graduate scholar award (2011). He was a leader of Missouri &ST team of AAPG Imperial Barrel Award Program (IBA) contest honorable mention (2009). He worked for ExxonMobil in Houston as a summer intern in the field of Geoscience in 2009.

He was involved in many non-academic activities inside and outside the campus. He voluntarily coached children soccer teams in Rolla for two years. He was in charge of the geophysical lab at Missouri &ST during the last two years. Hesham received Doctor of Philosophy degree in December 2012.